1

Effects of transport on a biomass burning plume from Indochina

during EMeRGe-Asia identified by WRF-Chem

Chuan-Yao Lin[1]*, Wan-Chin Chen[1], Yi-Yun Chien[1], Charles C. K. Chou[1], Chian-Yi Liu[1], Helmut Ziereis[2], Hans Schlager[2], Eric Förster[3], Florian Obersteiner[3], Ovid O. Krüger[4], Bruna A. Holanda[4], Mira L. Pöhlker[4,a], Katharina Kaiser[5,7], Johannes Schneider[5], Birger Bohn[8] , Klaus Pfeilsticker[9,10], Benjamin Weyland[10], Maria Dolores Andrés Hernández[6], John P. Burrows[6]

1. Research Center for Environmental Changes, Academia Sinica, Taipei, Taiwan
2. Deutsches Zentrum für Luft- und Raumfahrt (DLR), Institut für Physik der Atmosphäre, Oberpfaffenhofen, Germany
3. Karlsruhe Institute of Technology, Institute of Meteorology and Climate Research, Karlsruhe, Germany
4. Multiphase Chemistry Department, Max Planck Institute for Chemistry, Mainz, Germany
5. Particle Chemistry Department, Max Planck Institute for Chemistry, Mainz, Germany
6. Institute of Environmental Physics, University Bremen, Bremen, Germany
7. Institute for Atmospheric Physics, Johannes Gutenberg University, Mainz, Germany
8. Institute of Energy and Climate Research IEK-8, Forschungszentrum Jülich, Jülich, Germany
9. Heidelberg Center for the Environment, Heidelberg University, Heidelberg, Germany
10. Institute of Environmental Physics, Heidelberg University, Heidelberg, Germany

[a]now at: Faculty of Physics and Earth Sciences，Leipzig Institute for Meteorology, University of Leipzig/Experimental Aerosol and Cloud Microphysics Department, Leibniz Institute for Tropospheric Research, Leipzig, Germany

*Corresponding author
Chuan Yao Lin,
Research Center for Environmental Changes, Academia Sinica, Taipei, Taiwan
128 Sec. 2, Academia Rd, Nankang, Taipei 115, Taiwan
(E-mail: yao435@rcec.sinica.edu.tw, Tel.: +886-2-27875892, Fax: +886-2-27833584),

Abstract.

The Indochina biomass burning (BB) season in springtime has a substantial environmental impact on the surrounding areas in Asia. In this study, we evaluated the environmental impact of a major long-range BB transport event on 19 March 2018 (a flight of the HALO research aircraft, flight F0319) preceded by a minor event on 17 March 2018 (flight F0317). Aircraft data obtained during the campaign in Asia of the Effect of Megacities on the transport and transformation of pollutants on the Regional to Global scales (EMeRGe) were available between 12 March and 7 April 2018. In the F0319, results of 1-min mean carbon monoxide (CO), ozone (O₃), acetone (ACE), acetonitrile (ACN), organic aerosol (OA) and black carbon aerosol (BC) concentrations were up to 312.0 ppb, 79.0 ppb, 3.0 ppb, 0.6 ppb, 6.4 μg m^{-3}, 2.5 μg m^{-3} respectively, during the flight, which passed through the BB plume transport layer (BPTL) between the elevation of 2000–4000 m over the East China Sea (ECS). During F0319, CO, O₃, ACE, ACN, OA and BC maximum of the 1 minute average concentrations were higher in the BPTL by 109.0 ppb, 8.0 ppb, 1.0 ppb, 0.3 ppb, 3.0 μg m^{-3} and 1.3 μg m^{-3} compared to flight F0317, respectively. Sulfate aerosol, rather than OA, showed the highest concentration at low altitudes (<1000 m) in both flights F0317 and F0319 resulting from the continental outflow in the ECS.

The transport of BB aerosols from Indochina and its impacts on the downstream area was evaluated using a WRF-Chem model. The modeling results tended to overestimate the concentration of the species, with examples being CO (64 ppb), OA (0.3 μg m^{-3}), BC (0.2 μg m^{-3}) and O3 (12.5 ppb) in the BPTL. Over the ECS, the simulated BB contribution demonstrated an increasing trend from the lowest values on 17 March 2018 to the highest values on 18 and 19 March 2018 for CO, fine particulate matter (PM$_{2.5}$), OA, BC, hydroxyl radicals (OH), nitrogen oxides (NO$_x$), total reactive nitrogen (NO$_y$), and O₃; by contrast, the variation of J(O^{1}D) decreased as the BB

plume's contribution increased over the ECS. In the low boundary layer (<1000 m), the BB plume's contribution to most species in the remote downstream areas was <20 %. However, at the BPTL, the contribution of the long-range transported BB plume was as high as 30–80 % for most of the species (NO_y, NO_x, $PM_{2.5}$, BC, OH, O_3, and CO) over South China (SC), Taiwan, and the ECS. BB aerosols were identified as a potential source of cloud condensation nuclei, and the simulation results indicated that the transported BB plume had an effect on cloud water formation over SC and the ECS on 19 March 2018. The combination of BB aerosol enhancement with cloud water resulted in a reduction of incoming shortwave radiation at the surface in the SC and ECS by 5-7% and 2-4%, respectively, which potentially has significant regional climate implications.

1 Introduction

Biomass burning (BB) is one of the main sources of aerosols, greenhouse gases, and air pollutants (e.g. Ramanathan et al., 2007; Lin et al., 2009; 2014; Tang, 2003; Carmichael et al., 2003; Chi et al., 2010; Fu et al., 2012; Lin N.H. et al., 2012; Chuang et al., 2016). Reid et al. (2013) and Giglio et al. (2013) investigated the seasonal aerosol optical depth over Southeast Asia and have indicated that Indochina is a major contributor of carbon emissions in springtime. Galanter et al. (2000) estimated that BB accounts for 15–30 % of the entire tropospheric CO background. Huang et al. (2013) indicated that the contribution of BB in Southeast Asia to the aerosol optical depth (AOD) in Hong Kong and Taiwan could be in the range of 26-62 %. Moreover, BB emissions over Indochina are a significant contributor to black carbon (BC), organic carbon (OC), and O_3 in East Asia (Lin et al., 2014). In their BB modeling study, Lin et al. (2014) identified a northeast (NE) to southwest (SW) zone stretching from South China (SC) to Taiwan

89   with a reduction in shortwave radiation of approximately 20 W m^{-2} at the ground

90   surface. In addition, the total carbon emission from BB in Southeast Asia is

91   approximately 91 Tg C yr^{-1}, accounting for 4.9 % of the global total (Yadav et al.,

92   2017). According to Xu et al. (2018), BB in Indochina leads to BC production at high

93   concentrations of up to 2–6 µg m^{-3} in spring. The authors reported that BC particles

94   were transported to the glaciers in the Tibetan Plateau, where it significantly affected

95   the melting of the snow, causing some severe environmental problems, such as water

96   resource depletion. Ding et al. (2021) indicated that BB aloft aerosols strongly increase

97   the low cloud coverage over both land and ocean and affect the monsoon in the

98   subtropical Southeast Asia.

99   Although many researchers have indicated the importance of BB emissions, their

100   precise estimation and applying in the modeling study remains challenging (Fu et al.

101   2012; Huang et al. 2013; Pimonstree et al. 2018; Marvin et al. 2021). For example,

102   Heald et al. (2003) conducted an emission inventory in Southeast Asia and reported that

103   the uncertainties of BB emission estimations could be a factor of three or even higher.

104   Following an inverse model analysis, Palmer et al. (2003) also indicated the

105   overestimation of regional BB emissions over Indochina. Shi and Yamaguchi (2014)

106   pointed out BB emissions exhibited strong temporal interannual variability between

107   2001 and 2010 over southeast Asia. Satellite data can be used to easily locate hotspots

108   such as those where agricultural residuals burning and forest wildfires are occurring

109   worldwide. However, accurately quantifying the amount of BB emission from satellite

110   data is difficult because anthropogenic pollutants and BB emissions are typically mixed

111   in the atmosphere. During the NASA Transport and Chemical Evolution over the

112   Pacific (TRACE-P) aircraft mission in spring 2001, Jacob et al. (2003) observed that

113   warm conveyor belts (WCBs) lift both anthropogenic and BB (from SE Asia) air

114   pollution to the free troposphere, resulting in complex chemical signatures.

Wiedinmyer et al. (2011) demonstrated that the uncertainty of emission estimation could be as high as a factor of 2 because of the error introduced by estimates in fire hotspots, area burned, land cover maps, biomass consumption, and emission factors in the model. In this context, Lin et al. (2014) highlighted the uncertainty of emission estimation in the first version of Fire Inventory from NCAR (Wiedinmyer et al., 2011).

The transport of BB pollution is strongly dependent on the atmospheric structure and weather conditions. Tang et al. (2003) noted that most BB aerosols, having their source in Indochina (mainly south of 25 °N and be alofted to an altitude of 2000–4000 m) during the TRACE-P campaign were associated with outflow in the WCB region after frontal passage. Lin et al. (2009) suggested a mountain lee-side troughs as an important mechanism, resulting in BB product transport from the surface to >3000 m. BB pollution is often transported from its sources to the East China Sea (ECS), Taiwan, and the western North Pacific within a few days.

The airborne field experiment EMeRGe (Effect of Megacities on the transport and transformation of pollutants on the Regional to Global scales) over Asia was led by the University of Bremen, Germany and conducted in collaboration with Academia Sinica, during the inter-monsoon period in 2018 (http://www.iup.uni-bremen.de/emerge/home/home.html). The EMeRGe aircraft mission consists of two parts. The first mission phase was conducted in Germany in July 2017 and the second phase was conducted from Taiwan in 2018 (Andrés Hernández et al. 2022).EMeRGe in Asia aimed at the investigation of the long range transport (LRT) of local and regional pollution originating in Asian major population centers (MPCs) from the Asian continent into the Pacific. A central part of the project was the airborne measurement of pollution plumes on-board of the High Altitude and Long Range Research Aircraft (HALO). The HALO platform was based in Tainan, Taiwan (Fig. 1a-b), and made optimized transects and vertical profiling in regions north or south of Taiwan,

141 dependent on the relevant weather and emission conditions. HALO measurements

142 additionally provide important information for the evaluation of the LRT of BB

143 emissions and its potential environmental impact in East Asia between 12 March and 7

144 April 2018. During the EMeRGe-Asia campaign, HALO carried out 12 mission flights

145 in Asia and 4 transfer flights from Europe to Asia with a total of 110 flight hours.

146   This paper is organized as follows: the model configuration and BB emission

147 analysis employed in the model simulation are described in Section 2, and the weather

148 conditions and HALO measurement results are presented in Section 3. The model

149 performance, as well as the evaluation of BB product transport and effects on East Asia

150 selected regions are discussed in Sections 4 and 5, respectively.

151

152 **2 Aircraft data and Model configuration**

153 **2.1 HALO aircraft data**

154 The HALO aircraft was equipped with a number of instruments and a detailed

155 description of the measurement systems onboard the HALO was presented in Andrés

156 Hernández et al.(2022). In this study, aerosol data (OA, BC, SO_4^{2-}, NO_3^-, NH_4^+), and

157 trace gases such as CO, SO_2, O_3, NO_x, NO_y, acetone (ACE), acetonitrile (ACN), HCHO,

158 HONO, and photolysis rate $J(O^1D)$, $J(NO_2)$ were employed in the analysis.

159 **2.2   WRF-Chem Model and model configuration**

160 We used the Weather Research Forecasting with Chemistry (WRF-Chem) model (Ver.

161 4.1.1) (Grell et al., 2005; Powers et al. 2017) to study the LRT of air masses associated

162 with BB pollutants in Indochina. The initial and boundary meteorological conditions

163 for WRF-Chem were obtained from National Centers for Environmental Prediction

164 (NCEP)-GDAS Global Analysis data sets at 6-h intervals. The Mellor–Yamada–Janjic

165 planetary boundary layer scheme (Janjic, 1994) was applied. The horizontal resolution

166 for the simulations performed was 10 km, and the grid box had 442×391 points in the

167 east–west and north–south directions (Fig. 1a). A total of 41 vertical levels were

168 included, with the lowest level at an elevation of approximately 50 m. To improve the

169 accuracy of the meteorological fields, a grid nudging four-dimensional data

170 assimilation scheme was applied using the NCEP-GDAS Global Analysis data.

171 The cloud microphysics used followed the Lin scheme (Morrison et al., 2005). The

172 rapid radiative transfer model (Zhao et al., 2011) was used for both longwave and

173 shortwave radiation schemes. Moreover, land surface processes are simulated using the

174 Noah-LSM scheme (Hong et al., 2009). In terms of transport processes, we considered

175 advection by winds, convection by clouds, and diffusion by turbulent mixing. The

176 removal processes in this study were gravitational settling, surface deposition, and wet

177 deposition (scavenging in convective updrafts and rainout or washout in large-scale

178 precipitation). The kinetic preprocessor (KPP) interface was used in both of the

179 chemistry schemes of the Regional Atmospheric Chemistry Mechanism (RACM,

180 Stockwell et al., 1990). The secondary organic aerosol formation module, the Modal

181 Aerosol Dynamics Model for Europe (Ackermann et al., 1998)/Volatility Basis Set

182 (Ahmadov et al., 2012), was also employed in the WRF-Chem model. In RACM, the

183 "KET" represents acetone and higher saturated ketones (KET) (Stockwell et al. 1997).

184 According to Singh et al. (1994), BB and the primary anthropogenic emissions could

185 contribute 26% and 3%, respectively, to the atmospheric acetone sources. The model

186 configuration and physics and chemistry options are listed in Table 1.

187

188 **2.3 Emission Inventories**

189 Anthropogenic emissions, such as NO_x, CO, SO_2, nonmethane volatile organic

190 compounds, sulfate, nitrate, PM_{10}, and $PM_{2.5}$, were adopted on the basis of the emission

191 inventory in Asia – MICS-Asia III which is the year in 2010 (Li et al., 2020; Kong et

192 al., 2020). For BB emissions FINNv1.5 (https://www.acom.ucar.edu/Data/fire/) was

193 employed. FINN provided daily, 1000 m resolution, global estimates of the trace gas

194 and particle emissions from open BB, which included wildfires, agricultural fires, and

195 prescribed burning but not biofuel use and trash burning (Wiedinmyer et al., 2011). The

196 anthropogenic emissions in Taiwan were obtained from the Taiwan Emission Data

197 System (TEDS) which is the emission inventory of the air-pollutant monitoring

198 database of the Taiwan Environmental Protection Administration. The TEDS version

199 used for this study was V9.0 (2013) and contained data on eight primary atmospheric

200 pollutants: CO, NO, NO_2, NO_x, O_3, PM_{10}, $PM_{2.5}$, and SO_2.

201

202 **3 Characteristics of the field experiment**

203 **3.1 MODIS Aerosol optical depth and Weather conditions**

204 Figures 2a and b visualizes the numerous fire hotspots and high aerosol optical depth

205 on 17 March 2018 registered by the MODIS satellite. Indeed, a large number of BB fire

206 hotspots frequently occurred over Indochina during the springtime (Supplementary

207 Figure S1a) and the EMeRGe-Asia campaign (Supplementary Figure S1b). During the

208 EMeRGe-Asia campaign, a relatively weaker forest fire activity in the year 2018

209 (Figure S1a) than in the past decade (2011-2020) over Indochina. On 17 March 2018

210 at 06:00 UTC (14:00 LT; LT = UTC+8:00) the weather data indicated a series of high-

211 pressure systems in northern China and a separate high-pressure system over the Japan

212 sea (Fig. 2c). At 1000 hPa, a strong northerly continental outflow was identified over

213 southern Japan, the ECS, and Taiwan (Fig. 2d). On 19 March 2018, a new frontal

214 system was located from Korea to the Guangdong province in SC (Fig. 2e). On the

215 same day at 06:00 UTC, a discontinued flow was identified at the frontal zone to the

216 north of Taiwan in the ECS (Fig. 2f). In other words, Taiwan was located at the

217 prefrontal and warm conveyor area due to the surrounding southerly flow on 19 March

218 2018 at 06:00 UTC (Figs. 2e and 2f, respectively). The southerly wind was gradually

219   replaced by the northeasterly after another frontal passage on 20 March 2018 at 00:00

220   UTC (data not shown).

221   In the upper layer (700 hPa; Figs. 2g–2j), the flow pattern differed from that at the

222   near-ground surface (1000 hPa; Figs. 2d and 2f). A southwesterly strong wind, coming

223   from the east side of the Tibetan Plateau in SC, moving to the North Eats i.e. Korea, is

224   converted to a polar front wave flow in northeastern China and Korea on 17 March

225   2018 (Fig. 2g). This high-elevation northward strong wind belt distribution at 700 hPa

226   was associated with a corresponding lee-side trough at the east of the Tibetan Plateau,

227   whereas a ridge was noted over the east coast of China on the same day (Fig. 2h).

228   Consistent with the mechanism reported by Lin et al. (2009), once a significant lee-side

229   trough formed, it provided favorable conditions for the upward motion over the lee-side

230   of the Tibetan Plateau and brought BB emission to the free troposphere layer following

231   the strong wind belt transport to the downwind area. After the weather system moved

232   to the east, the north–south trough turned to SW–NE such that the strong wind belt was

233   in an approximately SW–NE direction and located between 20 and 30 °N on 19 March

234   2018 (Figs. 2i and 2j). In conclusion, the Indochina BB pollutants were driven by the

235   strong wind belt from Indochina, northward to SC on 17 March 2018 and then eastward

236   passing over Taiwan between 20 and 30 °N to the south of Japan on 19 March 2018.

237

238   **3.2   Characteristics of LRT BB to the ECS by WRF-Chem model**

239   Figure 3 shows latitude longitude plots of the simulated CO concentration

240   differences with and without BB emission at an elevation of 1000 m (Fig. 3a), mainly

241   in Indochina, SC, and the South China Sea on 17 March 2018. The ambient flow was

242   easterly and then northward from the South China Sea to SC at 1000 m elevation

243   between 00:00 and 12:00 UTC on 17 March 2018 (Fig. 3a-b). To identify the high CO

244   concentration in the South China Sea at 1000 meters in Figures 3a and b, the HYSPLIT

backward trajectories with multiple points by 1˚X1˚ in the area (110-115˚E, 17.5-22.5 ˚N) in the South China Sea started at 00 UTC 17 March 2018 as shown in Figure 3e. The locations and dates of fire hot spots were distributed randomly in Indochina Peninsula as shown in the supplementary Figure S1c. The backward trajectories in the South China Sea indicated air masses mainly transported 48-72 and even 96 hrs. In other words, there could be contributed by fires occurring between 100-110 E and 12-20 N (Myanmar, Laos, Thailand, and Vietnam) during 13-15 March 2018. The BB plume accumulated and persisted for an extended period in the lower part of the boundary layer on 17 and 19 March 2018 (Figs. 3a-b, and 4a-b). In contrast, the high CO concentration followed the southwesterly or westerly strong wind belt (Figs. 3c-d, and 4c-d) and its weather conditions (Fig. 2) at an elevation of 3000-m (700 hPa). Following the movement of the ridge and trough at the 700 hPa geopotential height (Fig. 2h and 2j), the associated strong wind belt turned to move eastward in the SW–NE direction between 17 and 19 March 2018. The BB plume transport over Indochina was affected by a fast-moving strong flow at 700 hPa (Fig. 2g and 2i), shifting the plume toward Taiwan and the ECS, during 17–19 March 2018. The backward trajectories in the East China Sea (ECS) started at 04 UTC on 19 March 2018 at 3000 m indicating air masses mainly transported 48-72 and even 96 hrs (15-17 March) ago from Indochina as shown in Figure 4e. The highest CO concentration contributed by the BB plume was >150 ppb, originally sourced from Indochina, and it was mainly transported northward on 17 March 2018 (Figs. 3c-d) and then covered a large area in East Asia at a CO concentration of >100 ppb on 19 March 2018 (Figs. 4 c-d). Figure 5 indicates simulation differences for the contribution of BB along an E–W cross-section at 30 °N at 16:00 UTC on 18 March 2018 (Fig. 5a) and 06:00 UTC on 19 March 2018 (Fig. 5b). We noted that a strong wind at 2000 m elevation and a high CO concentration (>70 ppb) due to BB at the BPTL. Moreover, the CO concentration attributed to BB was low at

271   the elevation of >4000 m on 19 March at 06:00 UTC (Fig. 5b), showing that the BB

272   pollutants mainly affect altitudes below 4000 m.

273

274   **3.3 Aircraft measurements**

275   Two HALO flights were scheduled to the ECS to measure the pollutants following the

276   continental outflow; the flights departed on 17 (Fig. 6a) and 19 (Fig. 7a) March 2018

277   and followed similar tracks. To indicate the measurement results along the flight path,

278   the 1-min average data is shown in Figures 6b and 7b.   On 17 March 2018, the flight

279   departed from Tainan (Fig. 1b) at 01:09 UTC (09:09 LT) first southbound and then

280   northward to the ECS (Fig. 6a). The elevation for sample collection was mainly <4000

281   m, where the CO concentration was found to be <200 ppb in most cases on that day

282   (Fig. 6b). At elevations between 2000 and 4000 m, the concentration of the major

283   aerosol components (i.e., OA, BC, SO_4^{2-}, NO_3^-, and NH_4^+) was mostly <2 µg m^{-3},

284   except just above western Taiwan after 08:00 UTC (Figs. 6a–6d). The peak

285   concentrations for OA, BC, SO_4^{2-}, NH_4^+, and NO_3^- were 3.4, 1.2, 2.1, and 0.7 µg m^{-3},

286   respectively, at the altitude between 2000 and 4000 m. SO_4^{2-} demonstrated the highest

287   concentration among the aerosol components, especially during 04:00–04:37 and

288   05:48–06:15 UTC (peaking at 5.1 µg m^{-3}) when the flight was north of 30 °N and an

289   elevation of <1000 m (Figs. 6a–6c). This result could be attributed to anthropogenic

290   pollution from the continental outflow (Lin et al. 2012) or probably part from Japan

291   contributed to the high sulfate concentration in the boundary layer over the ECS. As for

292   the trace gases such as ACE, ACN and O_3, their concentrations between 2000 and 4000

293   m were ranging between 1-2 ppb, 0.1-0.3 ppb, and 60-70 ppb (Fig. 6b), respectively,

294   implying minor influence over the ECS by the BB plume in this flight. Figure 6e

295   illustrates the 96-h backward trajectories, which identified the air mass origin starting

296   at 02:00 UTC, followed by 04:00, 06:00, and 09:00 UTC. The continental outflow

297 contributed to higher sulfate concentrations (3–5 µg m^{-3} at 33 °N) at 04:00 and 06:00

298 UTC (Figs. 6b, 6c, and 6e) at <1000 m along the flight path. In contrast, south of 25 °N

299 and above Taiwan, the local pollution and continental outflow are dominating sources

300 on 17 March 2018.

301 The HALO flight on 19 March 2018 departed at 00:19 UTC (08:19 LT). It was

302 bound northward and sampled air at an altitude of <4000 m most of the time, as shown

303 in Figures 7a and 7b. Figures 7c and 7d indicate the latitude-height variation of SO$_4^{2-}$

304 and OA mass concentrations along the flight path on 19 March 2018. As the flight left

305 Taiwan, it maintained an elevation of 3000 m during 01:00–02:00 UTC (Fig. 7a, 121–

306 126 °E) and then descended to <1000 m during 02:00–02:40 UTC (Fig. 7b). The OA

307 mass concentration was higher at 3000 m than at the low altitude during 01:00–03:00

308 UTC (Figs. 7b and 7d). In particular, CO, OA and BC exhibited a substantial peak

309 concentration of 312 ppb, 6.4 µg m^{-3} and 2.5 µg m^{-3} at 01:54 and 02:51 UTC at 26 °N,

310 125–126 °E, and an altitude of 2000–4000 m, where a BPTL was observed. The trace

311 gases such as ACE, ACN, and even O$_3$ (Fig. 7b) have consistent peak times in the BPTL

312 with concentrations of 3.0 ppb, 0.6 ppb, and 79 ppb, respectively. In this flight, SO$_4^{2-}$

313 had the second-highest concentration among the aerosol components (1–2.4 µg m^{-3};

314 Figs. 7b and 7c) upstream of Taiwan (25–27 °N) during 1:00–3:00 UTC.

315 In the northern part of the flight between 03:00 and 05:00 UTC at an elevation of

316 >3000 m, the aerosol component concentrations were all at their lowest level (Figs. 7b–

317 7d). During 05:00–07:00 UTC, the HALO aircraft flew back southward to 25 °N, where

318 high OA mass concentrations appeared again between 2000 and 4000 m (Figs. 7a, 7b,

319 and 7d). Sulfate was the species with the highest concentration between 05:30 and

320 06:30 UTC (Figs. 7b and 7c) when the flight's elevation was <1000 m in the lower

321 boundary between 25 and 27 °N (upstream of Taiwan). The reason explaining this

322 observation is that the transport of anthropogenic pollutants of continental origin takes

place mainly in the boundary layer (Figs. 7b–7d). Other aerosol species, such as NO_3^- and NH_4^+, demonstrated low concentrations, except when the elevation was <1000 m, where they ranged up to 1 $\mu g\ m^{-3}$ (Fig. 7b).

The 96-h HYSPLIT backward trajectory starting from the flight locations at 02:00–07:00 UTC (Fig. 7e) indicated that the air masses at elevations between 2000 and 4000 m were potentially transported from Indochina. North of 30 °N and at altitudes of >3000 m at 04:00 UTC, the concentrations of air pollutants (including OA, SO_4^{2-}, NO_3^-, and NH_4^+) were low (Figs. 7b and 7e) even though the air mass in the low boundary was sourced from SC and the Taiwan Strait. In general, the BPTL was mainly located south of 30 °N as presented by Carmichael et al. (2003), and Tang et al. (2003). However, the ACN still could be around 300ppt or less as the flight at the north of 30 ˚N (during 3:30-4:30 UTC) and could be recognized as the contribution of BB (Förster et al. 2022). In other words, it might still have BB products being transported to the north of 30 N under favorable weather conditions although the ACN concentration was low compared to the south of it at the layer of BPTL(between 2000 and 4000 m).   The fact that higher OA was observed rather in the higher altitudes than in the lower boundary also demonstrated the vertical distribution over the ECS.

Figure 8 displays the vertical distribution of the gases and major aerosol components found on the flights on 17 (blue) and 19 (green) March 2018 as well as the mean concentrations noted in the seven flights (on 17, 19, 22, 24, 26, and 30 March and 4 April 2018; red) to the ECS during EMeRGe-Asia. Figure 8 illustrates all profiles calculated as 1-min mean and every 500-m interval with one standard deviation (±σ). The number of the data points is displayed on the right side of each figure. The mean CO concentration profile demonstrated a decreasing trend from 240 ppb near the ground to 150 ppb at an altitude of 2500 m and 140–160 ppb at altitudes >6000 m (Fig. 8a). The concentration for 17 March 2018 (flight F0317) was similar to the mean

349 concentration profile, except for that at the <1500 m elevation in the lower boundary.

350 However, a higher CO concentration (40–80 ppb) enhancement was noted on 19 March

351 2018 (flight F0319) than the mean profile and flight F0317. The mean difference in CO

352 concentration between flights F0319 and F0317 was as high as 80 ppb at an elevation

353 of 3000-3500 m (Fig. 8a). Similarly, OA concentration was significantly higher in the

354 BPTL vertical distribution in flight F0319 than in the mean profile and flight F0317

355 (Fig. 8b). The mean OA concentration for the flight F0319 peaked at an elevation of

356 2000–2500 m, increasing to 2 μg m^{-3} more than in the mean profile and flight F0317.

357 Other aerosol components such as SO_4^{2-}, NH_4^+, and NO_3^- (Supplementary Fig. S2a-c)

358 also had a similar vertical distribution trend, but the concentration differences were

359 minor compared with OA concentrations. The magnitude of the maximum differences

360 between the flights F0319 and F0317 in the BPTL was 1.3, 0.7, and 0.4 μg m^{-3} for

361 SO_4^{2-}, NH_4^+, and NO_3^-, respectively. The maximum difference concentration of BC can

362 be as high as 1.2 μg m^{-3} at 2000-2500 m between the flights F0319 and F0317 (Fig.8c).

363 Regarding the variations in ACN (Fig. 8d) and ACE (Fig. 8e) in the BPTL, their

364 maximum mean concentrations in the flight F0319 were higher than those in the profile

365 of the flight F0317 by 0.18 and 0.9 ppb, respectively. In other words, flight F0319 had

366 a more significant impact on the CO, OA, BC, and volatile organic compound (VOC)

367 species such as ACN and ACE in the BPTL, which might account for the effect of BB

368 emission transport from Indochina. The ozone concentration was lower in both flights

369 F0317 and F0319 than in the mean profile at the elevations <2000 m (Fig. 8f). The

370 ozone titration by NO_x in the low boundary might also play a role. However, it was

371 approximately 5–7 ppb higher in the flight F0319 than in the flight F0317 between the

372 elevations of 1500 and 3000 m. In their downwind area, LRT of BB emissions might

373 increase this concentration further at the BPTL (Tang et al., 2003; Lin et al., 2014) and

374 also discussed in section 4. By contrast, the J value [J(O^{1}D)] (Fig. 8g) was higher for

flight F0317 than for F0319 in the elevation range 1000–3000 m, in line with high aerosol concentrations and associated cloud enhancement that typically lead to decreased photolysis frequencies [i.e., $J(O^1D)$] (Tang et al., 2003). Figure S3 (Supplementary) indicated the aircraft measurement for the J value (JO^1D) and CCN (Cloud Condensation Nuclei; at a constant instrument supersaturation of 0.38 %) along the flight on 19 March 2018. The CCN number concentration (per cm^3), was consistently increased with the aerosol species (such as OA) as the flight passed through the BPTL (2000-4000 m). Consistently, at altitudes >4000 m the presence of clouds below the aircraft led to greater J values.

The concentrations of other species such as NO_y (Fig.8h) and HONO (Supplementary Fig. S2d) were also greater in flight F0317 than in flight F0319 by 0.4-1.2 ppb and 10-34 ppt, respectively, in the low boundary (<1500 m). At the BPTL, the concentration of NO_y (1-2 ppb) in the flight F0319 was higher than in the flight F0317, but the difference was less than 0.6 ppb. The results from the TRACE-P campaign, which examined the Asian outflow of NO_y, also demonstrated large increases in NO_y concentrations (0.5-1 ppb) downwind from Asia. The NO_y consisted mainly of HNO_3 and peroxyacetyl nitrate (Miyazaki et al., 2003; Talbot et al., 2003).

4 Simulation results and discussion

4.1 Model performance and BB transport identification

Tables 2 and 3 and Fig. 9 plot the Pearson correlation coefficients between 5-min merged observations on board the HALO and the simulation for flights F0317 and F0319. Meteorological parameters such as potential temperature (theta), relative humidity (RH), and wind speed (WS) were all captured well by the model along the HALO flight path on the 2 days. The correlation coefficient (R) for meteorological parameters was high, ranging from 0.92 to 0.99 (Table 2). The strong correlation

401   indicates the high representativeness of the reanalysis of meteorological data used in

402   the simulation. Among the trace species and aerosol components, toluene (TOL), NO_x,

403   BC, OA, ketones (KET), HONO, SO_2, and HCHO demonstrated an R of >0.5 (good

404   correlation) and CO and O_3 showed an R of nearly 0.5 (Table 2). The simulation

405   performance was investigated in the BL (<1000 m; Fig. 9), at 2000–4000 m altitude

406   (Table 3 and Fig. 9) and for the whole period of both flights (Table 2 and Fig. 9; blue

407   dot). Even in the BPTL, the simulated meteorological parameters presented a good

408   correlation (R > 0.93), followed by OA, BC, KET, CO, O_3, NO_x as well as NH_4^+ and

409   NO_y (R > 0.5) (Table 3). In other words, at the BPTL, the R for the simulation

410   significantly increased for OA, BC, CO, O_3, NO_y and KET (Tables 2 and 3 and Fig. 9),

411   which are indicators for BB being a source of pollution in the model. In contrast, SO_4^{2-},

412   NO_3^-, SO_2, NO_x, TOL, XYL, HCHO and HONO had better correlation in the lower part

413   of the boundary layer, at altitudes <1000 m (see Fig. 9) than in the BPTL. We explain

414   this by the transport of anthropogenic pollutants in the continental outflow in the lower

415   part of the boundary layer in ECS.

416   The modeling results tended to overestimate the concentration of the species, with

417   examples being CO (64 ppb), OA (0.3 µg m^{-3}), BC (0.2 µg m^{-3}) and O_3 (12.5 ppb;

418   Table 3) in the BPTL. Because high concentrations of CO, BC and OA in BPTL are

419   accurate indicators of BB in the model, the BB emission from the source of FINN data

420   are probably also overestimated (Lin et al., 2014). Except for OA and BC, the

421   correlations for other aerosol components such as NO_3^-, and SO_4^{2-} were poor (0.13 and

422   0.2, respectively). The poor correlation for SO_4^{2-} may result from the large uncertainty

423   in the emission of SO_2.

424   Because the meteorological parameters were simulated well, the simulation

425   discrepancies for chemical species are either caused by the emission estimation

426   uncertainties or by inaccuracies in the simulation of chemical oxidation processes

during LRT. Because CO, OA, and BC are accurate indicators of simulated BB

transport from Indochina (Carmical et al., 2003), the airborne measurements on board

the HALO are used as reference to evaluate the performance of the model for the flight

F0319 (Fig.10). The 5-min merged simulation of CO concentration with (blue line) and

without (green line) BB was compared to that measured on board the HALO (red line);

the concentration was mostly in the range of 100–200 ppb, with its peak approaching

300 ppb (at 01:50, 02:50, and 04:00 UTC) at the BPTL (Fig. 10a). In general, the

simulation captured the CO variation along the flight path. However, it overestimated

the observations by nearly 100 ppb for the simulation with BB at the BPTL during

01:00–02:00, 03:40–04:20, 05:00–05:40, and 06:30–07:20 UTC (Fig.10a). Notably, the

simulation difference was minor when the flight was in the lower part of the boundary

layer (02:30 and 06:00 UTC) i.e. < 1000m or at elevations of >4000 m (03:00–03:30

and 04:20–05:00 UTC). The model underestimated CO concentration in the lower part

of the boundary (<1000 m) (02:30 and 05:50–06:30 UTC) over the ECS. In conclusion,

our model simulation overestimates BB emissions but underestimates continental CO

emissions from China due to the underestimation of the emission inventory of the

MICS-Asia III (Kong et al.,2020) was adopted in this study.

OA and BC are also important BB indicators and were reasonably captured by the

model before 03:00 UTC when the flight was south of 28 °N at elevations of <4000 m

(Fig.10 b-c). The time series of simulated OA and BC has peak concentrations of nearly

4-5.5 μg m^{-3} and 2 μg m^{-3}, respectively, during HALO shuttle flights passing through

the BPTL (2000–4000 m) around 01:50 and 02:50 UTC. When BB emission was not

included in the simulation, the concentration peaks were not observed (see Fig. 10b-c,

450 green plot). Similar to the simulated CO results, the simulated OA and BC overestimate

451 the amounts of these species to the north of 28 °N during 03:30-04:20 UTC (Fig. 7a

452 and 10). Furthermore, when the simulation only considered direct effect (case ROCD,

453 purple), the overestimations were increased as shown in Figure 10b-c. As mentioned

454 earlier, a frontal system was just located from the ECS to SC (Fig. 2e) on 19 March

455 2018. In other words, the effect of wet scavenging reduced the aerosol concentration

456 bias in the ECS and SC, as for the frontal system providing the moist air mass in the

457 event flight F0319. The model after 07:30 UTC, which was related to local emissions

458 before HALO landed over western Taiwan on 19 March 2018. In general, our model

459 simulation captured reasonably well OA and BC with an R of 0.61 and 0.74,

460 respectively. A minor mean bias for OA (BC) is 0.3 µg m^{-3} (0.1 µg m^{-3}) and the root

461 mean square error (RMSE) of OA (BC) is 1.1 µg m^{-3} (0.4 µg m^{-3}) (Table 2). The R for

462 OA (BC) reached 0.85(0.79), with an RMSE of 0.7 µg m^{-3} (0.5 µg m^{-3}) when we

463 calculated the BB transport layer only between 2000 and 4000 m (Table 3 and Fig. 9).

464 In addition to OA and BC, simulated aerosol species such as SO_4^{2-} was overestimated,

465 whereas NO_3^- was underestimated although their concentrations were low (Table 3).

466 Because the BPTL was mainly between altitudes of 2000 and 4000 m, the subsequent

467 discussion focuses on the influence of the BPTL from Indochina on the downstream

468 areas, particularly the ECS and Taiwan.

4.2 Effects of LRT BB plume from Indochina on East Asia

To investigate the regional impacts of BB plume transport from Indochina, we compared the simulation with and without BB emission for the events on 17 and 19 March 2018. The analysis of the calculations focused on the impact over SC, Taiwan and ECS. These three selected regions are SCA (in South China), TWA (covered the whole Taiwan), and ECSA (in the ECS) as shown in Figure 1a. After being emitted the BB pollutants from Indochina were then transported northward to China and subsequently northeastward. The exact flow pattern depended on the weather conditions and flow types (ridge or trough) at 700 hPa (3000 m) between 17 and 19 March 2018 (see Fig. 2). Consequently, we investigated the hourly variation in the area mean concentrations or mixing ratios of air pollutant trace constituents to assess the importance of BB emissions from Indochina on the selected downstream region e.g. the ECSA (Fig. 11), SCA, TWA and ECSA (Table 4). The contribution of CO (or others species) due to BB was estimated by the difference between simulations with and without the BB emission. These differences are then expressed as a fraction in percentage shown in Figure 11 (blue line). The mean concentration of CO (red line) over the ECSA (Fig. 11a) was at its lowest (115 ppb) on 17 March 2018; it gradually increased to a peak concentration of 280 ppb on 18 March 2018 and then remained stable at 260 ppb on 19 March 2018. The contribution of CO from BB (blue line) ranged from 19 % (<22 ppb) on 17 March 2018 to a peak of 42 % (~113 ppb) on 18 March 2018 and then gradually declined to 26 % on 19 March 2018 (Fig. 11a). As for OA (BC), the lowest percent contribution by BB was 14-16% (<5%) between 16 and 17 March 2018 while the highest could be more than 40% (80%) during 18 and 19 March 2018 (Fig. 11b and c). The BB contributed to $PM_{2.5}$ was 19 % (0.39 µg m^{-3}) on 17 March 2018 (Fig. 11d), increasing to 45 % (3.6 µg m^{-3}) on 18-19 March 2018 because the BB plume spread by the strong wind to the ECSA.

495   The variation of O_3 (Fig. 11e) depends on transport and photochemistry, which

496   involves the precursors NO_x and VOC and the photolysis frequency of NO_2, $J(NO_2)$.

497   For the elevations between 2000–4000 m, O_3 changes are similar to those of CO, NO_x

498   and KET, which were mainly contributed by the LRT BB plume and related to the

499   ozone precursor after 18 March 2018. The lowest and highest O_3 concentrations on 17

500   and 18 March 2018 were 56 and 75 ppb, respectively, of which we estimate that 5.6

501   ppb (10 %) and 34 ppb (45 %) were BB's contributions, respectively. Although the

502   mean NO_x concentration was relatively small (0.06–0.18 ppb), the BB contributed 35–

503   70 % (0.02–0.13 ppb) during 17–19 March 2018 (Supplementary Fig. S4a). The KET

504   concentration was in the range 0.4 to 2.7 ppb, with BB contributing nearly 20–26 %

505   (0.08–0.7 ppb) during 17–19 March 2018 (Supplementary Fig. S4b).

506   The area-mean OH contributed by BB increased from its lowest level (<30 %) on

507   17 March 2018 to its highest (nearly 70 %) on 19 March 2018 (Fig. 11f). HO_2 also has

508   an increasing trend from 10 % to 40 % during daytime over the period 17–19 March

509   2018 (Supplementary Fig. S4c). The amounts of the oxidizing agent, OH, and the free

510   radical HO_2 depend on the amounts of trace gases, which produce and remove these

511   radicals, (eg. NO_x, water vapor, ozone, hydrocarbons, etc.) and the relevant photolysis

512   frequencies $J(O_3 \rightarrow O^1D)$, $J(NO_2)$ etc.. However, BB's contribution to photolysis

513   frequencies $J(O_3 \rightarrow O^1D)$ (Fig. 10g), $J(NO_2)$ (Supplementary Fig. S4d) etc. decreased

514   as the mean BB aerosol concentration increased over the ECS during 17–19 March

515   2018. This is because photolysis calculation results used simulated aerosol and cloud

516   formation, which increased over the ECSA (Fig. 13).

517   The NO_y, mean concentration ranged from 1.0 to 4.5 ppb, of which BB's

518   contribution was from 55 to 82 % (Supplementary Fig. S4e). Such a high contribution

519   from BB also demonstrated the effects of long-distance transport. Figure 11h indicates

520   an increasing trend of HCHO concentration from 17 to 19 March 2018. HCHO

521 formation and destruction depend on the rate of reaction of OH with HCHO precursors

522 and the rate of reaction of HCHO with OH and the photolysis frequency of HCHO. As

523 a result, HCHO production varied with OH concentration. The lowest and highest

524 concentrations of HCHO were on 17 and 19 March 2018, respectively.   In summary,

525 the consistent variations in BB contributions to CO, OA, BC, $PM_{2.5}$, OH, HCHO, NO_x,

526 NO_y, and O_3 peaked on 18 or 19 March 2018, whereas $J(O^1D)$ decreased between 17

527 and 19 March 2018.

528   Figure 12 displays the fraction in % that the long-range transported BB emission

529 contributes to the amounts of NO_x, NO_y, $PM_{2.5}$, OA, BC, OH, O_3, CO, KET, HO_2,

530 HCHO and $J(O^1D)$, over the ECSA on 17 and 19 March 2018. Except for NO_y, BB

531 contribution was generally <11 % at elevations of <1000 m over the ECSA. The scatter

532 distribution of the simulation results indicates that the effect of BB emission at

533 elevations of <1000 m (Fig. 12a) was significantly lower than that between the

534 elevations of 2000 and 4000 m (Fig. 12b). For NO_y, NO_x, $PM_{2.5}$, BC, OH, O_3, and CO,

535 the BB contribution was >30 % at the elevation of 2000–4000 m over the ECSA (Fig.

536 12b). Table 4 further summarizes the effect of BB emission on the downwind areas

537 (SCA, TWA, and the ECSA) at the <1000 m and 2000–4000 m elevations. The

538 contribution of BB to NO_y, NO_x, $PM_{2.5}$, BC, OH, O_3 and CO was at least 30–80 % at

539 the elevation of 2000–4000 m over the regions SCA, TWA and ECSA (Table 4). In the

540 lower boundary layer (i.e. <1000 m), the BB contribution for most species at the remote

541 downstream areas was <20 %, except for TWA. Because of the high mountains (Lin et

542 al. 2021) present in TWA, the BB plume passing over Taiwan was potentially

543 transported downward through mountain–valley circulation to the lower boundary layer

544 (Ooi et al., 2021). The influence of BB over TWA was the highest among these three

545 downstream regions (see Table 4) as its location was directly on the transport pathway

546 for the BB plume on the major event day (flight F0319).

547   Figure 13a displays the simulated cloud water difference with and without BB

548   emission over different regions on 17 and 19 March 2018. BB aerosols are a potential

549   source of cloud nuclei. The simulations show the impact of BB on cloud water

550   enhancement (Fig. 13a) in the vertical distribution. Cloud water enhancement over SCA

551   was associated with aerosol enhancement from the BB in the altitude range 1000–4000

552   m: the peak being 1.8-2.0 mg kg^{-1} at 2000 m on these 2 days (Fig. 13a). The abundance

553   of BB emissions transported from Indochina to SCA (Figs. 3 and 4) is expected to

554   contribute to the high cloud water formation over SCA. Furthermore, the southerly flow

555   (Figs. 3 and 4) that transports warm and moist air mass from the South China Sea may

556   have favored cloud formation in flights F0317 and F0319. High cloud water related to

557   BB can be seen in the simulations of these two days. In the remote ECSA regions, the

558   cloud water substantially increased on 19 March 2018 (Fig. 13a) compared to 17 March

559   2018 because of a significant difference in BB emissions transported to the ECSA

560   between 17 and 19 March 2018 (Figs. 3 and 4). Similarly, the cloud water enhancement

561   over Taiwan also only appeared on 19 March 2018 (Fig. 13a). Furthermore, nearly no

562   difference in the cloud water vertical distribution over the region IDCA (Fig. 1a) in

563   Indochina was noted because in the Indochina region, spring is the dry season (Lin et

564   al., 2009) and thus unfavorable for cloud water formation. Figure 13b shows the cloud

565   water difference when the aerosol indirect effect turned off in the simulation over

566   different regions on 19 March 2018. The significant cloud water shortage over ECSA,

567   and SCA could be as high as 2.4 mg/kg and 1.5 mg/kg, respectively (Fig.13b). In other

568   words, the role of the chemistry-microphysics interactions (indirect effect) plays an

569   important role in the cloud water enhancement in the SCA and ECSA in this study.

570   The simulated downward shortwave flux at the noontime at ground surface due

571   to BB was 2-4% and 5-7% reduction over the regions ECSA and SCA, respectively,

572   (supplementary Fig. S5a-b, blue line) during 18-19 March 2018. However, a significant

573 shortwave flux reduction at the noontime at ground surface could be 15-20% due to

574 aerosol indirect effect in the region SCA during 18-19 March 2018 (supplementary Fig.

575 S5a-b blue dashed line). The combination of BB aerosols enhancement and increased

576 cloud water results in shortwave radiation reduction, implying the possibility of

577 regional climate change in East Asia driven by BB aerosols.

578

579 **5. Summary**

580 The BB during spring in Indochina has a significant impact on the chemistry and

581 composition of the troposphere in the surrounding regions of East Asia. During the

582 EMeRGe campaign in Asia, atmospheric pollutants were measured on board the HALO

583 aircraft. In this study, a minor long-range BB transport event was observed from

584 Indochina on 17 March 2018 (flight F0317), followed by a major long-range BB

585 transport event on 19 March 2018 (flight F0319). The impact on tropospheric trace

586 constituent composition and the environment has been investigated.

587 During the major BB transport event F0319, the 1-min mean of the peak

588 concentrations of the trace constituents CO, O3, ACE, ACN, OA and BC between the

589 altitudes of 2000 and 4000 m over the ECS were 312.0 ppb, 79.0 ppb, 3.0 ppb, 0.6 ppb,

590 6.4 µg m^{-3}, 2.5 µg m^{-3} respectively. In comparison during the F0317 event CO, O3,

591 ACE, ACN, OA and BC were 203.0 ppb, 71.0 ppb, 2.0 ppb, 0.3 ppb, 3.4 µg m^{-3}, 1.2

592 µg m^{-3} respectively.

593 When the elevation was <1000 m for both the F0317 and F0319 events, the sulfates,

594 rather than OA, had the highest concentrations. The peak concentration could be as high

595 as 5.1 µg m^{-3} in the low boundary for the event F0317 in the ECS. This observation is

596 most likely explained by a continental outflow from regions having fossil fuel

597 combustion in the lower boundary layer over the ECS.

598 In this study, the WRF-Chem model was employed to evaluate the BB plume

599　transported from Indochina and its influence on the downstream areas including South

600　China, Taiwan, and the ECS. The contribution of the BB plume for most species in the

601　remote downstream areas was <20 % in the lower boundary layer (altitude <1000 m).

602　In comparison, the contribution of long-range transported BB plume was 30–80 %, or

603　even higher, for many of the trace constituents (NO_y, NO_x, CO, OH, O_3, BC and $PM_{2.5}$)

604　in the altitude range between 2000 and 4000 m for SC, Taiwan, and the ECS. The large

605　influence of BB over Taiwan is most probably because the BB transport passes directly

606　over Taiwan.

607　　BB aerosols are potential sources of cloud nuclei. The WRF simulations estimate

608　the effect of the BB plume on cloud water formation over SC and the ECS. We observe

609　in the simulations cloud water enhancement over SC at elevations of 1000–4000 m.

610　This increase of cloud water is consistent with an increase in aerosol, caused by BB

611　emissions, transported from Indochina to SC. In remote regions of the ECS, the

612　simulated cloud water was significantly larger during the major BB event on 19 March

613　2018 than the minor BB event on 17 March 2018. The simulated decrease of the

614　photolysis frequency ($J(O^1D)$ and J (NO_2)) is attributed to the difference in aerosol

615　concentrations and associated cloud enhancement between the two events over the ECS.

616　This we explain by the significant differences in BB emissions transported to the ECS

617　between the two events. The simulated downward shortwave flux at the noontime at

618　ground surface due to BB was 2-4% and 5-7% reduction over the regions ECS and SC,

619　respectively. The combination of increased BB aerosol concentration and increased

620　amounts of cloud water led to reductions in the amount of incoming shortwave radiation

621　at the surface over the ECS and SC. This influences tropospheric chemistry and

622　composition, regional climate, precipitation, ocean biogeochemistry, agriculture, and

623　human health.

624

Author contribution

CYL conceived the idea, analyzed the data, writing and editing of the manuscript. WNC and YYC run the model and analyzed the data. CKC joined the manuscript discussion.CYLiu provided the MODIS data. HZ and HS provided trace gases data. EF provided acetonitrile data. FO performed the ozone measurement. OOK, BAH and MLP were responsible for the BC measurement. KK and JS were responsible for C-ToF-MS measurements. KP and BW provided HONO data. JPB and MDAH led the EMeRGe-Asia experiment. All authors have read and agree to the published version of the manuscript.

Competing interests

The authors declare that they have no conflict of interest.

References:

Ackermann, I. J., Hass, H., Memmsheimer, M., Ebel, A., Binkowski, F. S., and Shankar, U.: Modal aerosol dynamics model for Europe: development and first applications, Atmos. Environ., 32, 2981–2999, https://doi.org/10.1016/S1352-2310(98)00006-5, 1998.

Ahmadov, R., McKeen, S. A., Robinson, A. L., Bahreini, R., Middlebrook, A. M., de Gouw, J. A., Meagher, J., Hsie, E.- Y. Edgerton, E., Shaw, S., and Trainer, M.: A volatility basis set model for summertime secondary organic aerosols over the eastern United States in 2006, J. Geophys. Res., 117, https://doi.org/10.1029/2011JD016831, 2012.

Andrés Hernández, M. D., Hilboll, A., Ziereis, H., Förster, E., Krüger, O. O., Kaiser, K., Schneider, J., Barnaba, F., Vrekoussis, M., Schmidt, J., Huntrieser, H., Blechschmidt, A.-M., George, M., Nenakhov, V., Harlass, T., Holanda, B. A., Wolf, J., Eirenschmalz, L., Krebsbach, M., Pöhlker, M. L., Kalisz Hedegaard, A. B., Mei, L., Pfeilsticker, K., Liu, Y., Koppmann, R., Schlager, H., Bohn, B., Schumann, U., Richter, A., Schreiner, B., Sauer, D., Baumann, R., Mertens, M., Jöckel, P., Kilian, M., Stratmann, G., Pöhlker, C., Campanelli, M., Pandolfi, M., Sicard, M., Gómez-Amo, J. L., Pujadas, M., Bigge, K., Kluge, F., 770 Schwarz, A., Daskalakis, N., Walter, D., Zahn, A., Pöschl, U., Bönisch, H., Borrmann, S., Platt, U. and Burrows, J. P.: Overview: On the transport and transformation of pollutants in the outflow of major population centres –observational data from the EMeRGe European intensive operational period in summer 2017. Atmos. Chem. Phys., 22, 5877–5924, https://doi.org/10.5194/acp-22-5877-2022, 2022.

Carmichael, G. R., Tang,Y., Kurata, G., Uno, I., Streets, D., Woo, J.-H., Huang, H., Yienger, J., Lefer, B., Shetter R. et al.: Regional-scale chemical transport modeling in support of the analysis of observations obtained during the TRACE-P experiment, J. Geophys. Res., 108(D21), 8823, doi:10.1029/ 2002JD003117, 2003.

Chuang, M.T., Fu, J.S., Lee, C.T., Lin, N.H., Gao, Y.,Wang, S.H., Sheu, G.R., Hsiao, T.C., Wang, J.L., Yen, M.C., Lin, T.H. and Thongboonchoo, N.: The simulation of long-range transport of biomass burning plume and short-range transport of anthropogenic pollutants to a mountain observatory in East Asia during the 7-SEAS/2010 Dongsha Experiment. Aerosol Air Qual. Res. 16: 2933–2949, 2016.

Chi K H., C. Y. Lin, C.F.Ouyang, J.Lin Lin, N.H. Lin, G.R. Sheu, C. T. Lee: PCDD/F Measurement at a High-altitude Station in Central Taiwan: Evaluation of Long-range Transport of PCDD/Fs during the Southeast Asia Biomass Burning Event, *Environmental Science & Technology*,*44,2954-2960*, DOI: 10.1021/es1000984 https://doi.org/10.1021/es1000984, 2010.

Ding K., Huang X., Ding A., Wang M., Su H., et al.: Aerosol-boundary-layer-monsoon interactions amplify semi-direct effect of biomass smoke on low cloud formation in Southeast Asia., Nature Communications, 12:6416, 2021.

Förster, E., Bönisch, H., Neumaier, M., Obersteiner, F., Zahn, A., Hilboll, A., Kalisz Hedegaard, A. B., Daskalakis, N., Poulidis, A. P., Vrekoussis, M., Lichtenstern, M., and Braesicke, P.: Chemical and dynamical identification of emission outflows during the HALO campaign EMeRGe in Europe and Asia, Atmos. Chem. Phys. Discuss. [preprint], https://doi.org/10.5194/acp-2022-455, in review, 2022.

Fu, J. S., Hsu, N. C., Gao, Y., Huang, K., Li, C., Lin, N.-H., and Tsay, S.-C.: Evaluating the influences of biomass burning during 2006 BASE-ASIA: a regional chemical transport modeling, Atmos. Chem. Phys., 12, 3837–3855,

698   https://doi.org/10.5194/acp-12-3837-2012, 2012.

699 Galanter, M., Levy, H., Carmichael, G. R.: Impacts of biomass burning on tropospheric
700   CO, NOx, and O3, J. Geophys. Res. Atmos., 105, 6633-6653, 2000.

701 Giglio, L., Randerson, J.T., Werf, G.R.V.D.: Analysis of daily, monthly, and annual
702   burned area using the fourth-generation global fire emissions database (GFED4). J.
703   Geophys. Res. Biogeosci. 118 (1), 317–328., 2013.

704 Grell, G. A., Peckham, S. E., Schmitz, R., McKeen, S. A., Frost, G., Skamarock, W. C.,
705   and Eder, B.: Fully coupled "online" chemistry within the WRF model, Atmos.
706   Environ., 39, 6957–6975, https://doi.org/10.1016/j.atmosenv.2005.04.027, 2005.

707 Heald, C. L., Jacob D.J., Fiore, A.M., Emmons, L. K., et al.: Asian outflow and trans-
708   Pacific transport of carbon monoxide and ozone pollution: An integrated satellite,
709   aircraft, and model perspective, J. Geophys. Res., 108(D24), 4804,
710   doi:10.1029/2003JD003507, 2003.

711 Hong, S., Lakshmi V., Small, E.E., Chen, F., Tewari, M., Manning, K.W.: Effects of
712   vegetation and soil moisture on the simulated land surface processes from the
713   coupled WRF/Noah model. J Geophys Res 114(D18), D18118, 2009.

714 Huang, K., Fu, J. S., Hsu, N.C., Gao, Y., Dong, X., Tsay, S. C., Lam, Y. F.: Impact
715   assessment of biomass burning on air quality in Southeast and East Asia during
716   BASE-ASIA, Atmospheric Environment, 78, 291e302, 2013.

717 Jacob, D.J., Crawford, J. H. Kleb, M. M.,Connors, V. S, Bendura, R. J., Raper, J. L.,
718   Sachse,G. W., Gille, J. C., Emmons, L., Heald, C. L.: The transport and chemical
719   evolution over the pacific (trace-P) aircraft mission: design, execution, and first
720   results. J. Geophys. Res. Atmos. 108 (D20), 2003.

721 Janjic, Z.I.: The step-mountain eta coordinate model: further developments of the
722   convection,viscous layer, and turbulence closure schemes, Mon.Wea. Rev., 122,
723   927–945, 1994.

724 Kong L., Tang X., Zhu J., Wang Z., Fu J.S., Wang X., et al.: Evaluation and uncertainty
725   investigation of the NO2, CO and NH3 modeling over China under the framework
726   of MICS-Asia III. Atmos. Chem. Phys., 20, 181–202, 2020.
727   https://doi.org/10.5194/acp-20-181-2020

728 Li, J., Nagashima,T., Kong, L., Ge, B., Yamaji, K., Fu, J. S., Wang X., Fan, Q., Itahashi ,
729   S.,et al.: Model evaluation and inter-comparison of surface-level ozone and relevant
730   species in East Asia in the context of MICS-ASIA phase III Part I: overview. Atmos.
731   Chem. Phys., 19, 12993–13015, https://doi.org/10.5194/acp-19-12993-2019, 2019.

732 Lin, C.Y., Hsu, H.M., Lee, Y.H., Kuo, C. H., Sheng, Y.F., Chu, D. A.: A new transport
733   mechanism of biomass burning from Indochina as identified by modeling studies.,
734   *Atmos. Chem. Phys.*, 9, 7901-7911. https://doi.org/10.5194/acp-9-7901-2009 ,2009.

735 Lin, C. Y., Chou, C.C.K, Wang, Z., Lung, S.C., Lee, C. T., Yuan, C.S., Chen, W. N.,

Chang, S. Y., Hsu, S. C., Chen, W. C., Liu, Shaw. C.: Impact of different transport mechanisms of Asian dust and anthropogenic pollutants to Taiwan. Atmospheric Environment, 60,403-418, http://dx.doi.org/10.1016/j.atmosenv.2012.06.049, 2012.

Lin, C. Y., Zhao, Liu, C. X, Lin, N. H., Chen, W. N.: Modeling of long-range transport of Southeast Asia biomass burning pollutants to Taiwan and their radiative forcing over East Asia, *Tellus B, 66, 1-17. 23733. http://dx.doi.org/10.3402/tellusb.v66.23733, 2014.*

Lin, C.Y., Sheng, Y. F., Chen, W. C., Chou, C.C. K., Chien, Y. Y., Chen, W. M.: Air quality deterioration episode associated with typhoon over the complex topographic environment in central Taiwan. Atmos. Chem. Phys., 21, 16839-16910. https://doi.org/10.5194/acp-21-16893-2021, 2021.

Lin, N.H., Tsay, S.C., Reid, J. S.,Yen, M.C., Sheu, G. R.,Wang, S.H., Chi, K.H.,et al. : An overview of regional experiments on biomass burning aerosols and related pollutants in Southeast Asia: From BASE-ASIA and Dongsha Experiment to 7-SEAS. Atmos. Environ. 78: 1–19, 2012.

Marvin, M. R., Palmer P. I., Latter, B. G., Siddans, R., Kerridge, B.J., Latif, M. T., Khan, M. F.: Photochemical environment over Southeast Asia primed for hazardous ozone levels with influx of nitrogen oxides from seasonal biomass burning. Atmos. Chem. Phys., 21, 1917–1935. https://doi.org/10.5194/acp-21-1917-2021, 2021.

Miyazaki Y., Kondo Y., Koike M., Fuelberg H. E., Kiley C. M., Kita K., Takegawa N., Sachse G. W., Flocke F., Weinheimer A. J., Singh H. B., Eisele F. L., Zondlo M., Talbot R. W., Sandholm S. T., Avery M. A., Blake D. R.: Synoptic-scale transport of reactive nitrogen over the western Pacific in spring, J. Geophys. Res., 108(D20),8788, doi:10.1029/2002JD003248., 2003.

Morrison H., Curry, J.A., Khvorostyanov,V.I.: A new double-moment microphysics parameterization for application in cloud and climate model. PartI: Description. *Journal of the Atmospheric Sciences.*, 62, 1665-1676, 2005.

Neu, J. L., and Prather, M. J.: Toward a more physical representation of precipitation scavenging in global chemistry models: Cloud overlap and ice physics and their impact on tropospheric ozone. Atmo. Chem. and Phys., 12, 3289–3310. https://doi.org/10.5194/acp-12-3289-2012 ,2012

Palmer, P. I., Jacob, D. J., Jones, D. B. A., Heald, C. L., Yantosca, R. M., Logan, J. A., Sachse, G. W. and Streets, D. G.: Inverting for emissions of carbon monoxide from Asia using aircraft observations over the western Pacific, *J. Geophys. Res*., 108(D21), 8828, doi:10.1029/2003JD003397, 2003.

Pimonsree, S., Vongruang, P., Sumitsawan, S.: Modified biomass burning emission in modeling system with fire radiative power: Simulation of particulate matter in Mainland Southeast Asia during smog episode. *Atmospheric Pollution Research*, 9,

774   133-145.   http://dx.doi.org/10.1016/j.apr.2017.08.002, 2018.

775 Powers G., J. B. Klemp, W. C. Skamarock, C. A. Davis, J. Dudhia, D. O. Gill, et al.The

776   weather research and forecasting model Overview, System Efforts, and Future

777   Directions. Bulletin of the American Meteorological Society, 98,1717-1737, 2017.

778 Ramanathan, V., Ramana, M. V., Roberts, G., Kim, D., Corrigan, C., Chung, C., and

779   Winker, D.: Warming trends in Asia amplified by brown cloud solar absorption.

780   *Nature*, 448, 575-U575, 2007.

781 Reid, J. S., Hyer, E. J., Johnson, R. S., Holben, B. N., Yokelson, R. J., Zhang, J., et al. :

782   Observing and understanding the Southeast Asian aeroslo system by remote sensing:

783   An initial review and analysis for the Seven Southeast Asian Studies (7SEAS)

784   program, Atmospheric Research, 122, 403-468, 2013.

785 Shi, Y., Yamaguchi, Y.: A high-resolution and multi-year emissions inventory for

786   biomass burning in Southeast Asia during 2001-2010. Atmospheric Environment,

787   98, 8-16,   http://dx.doi.org/10.1016/j.atmosenv.2014.08.050, 2014.

788 Singh H.B., Hara D.O., Herlth D., Sachse W., Blake D.R., Bradshaw J.D., Kanakidou

789   M., Crutzen P. J., Acetone in the atmosphere: Distribution, sources, and sink., J.

790   Geophys. Res., 99,1805-1819, 1994.

791 Stein, A. F., R. R. Draxler, G. D. Rolph, B. J. B. Stunder, M. D. Cohen, and F.

792   Ngan. : NOAA's HYSPLIT Atmospheric Transport and Dispersion Modeling

793   System, Bulletin of the American Meteorological Society 96, 12 (2015): 2059-

794   2077, https://doi.org/10.1175/BAMS-D-14-00110.1, 2021.

795 Stockwell, W. R., Middleton, P., Chang, J. S., and Tang, X.: The second generation

796   regional acid deposition model chemical mechanism for regional air quality

797   modeling, J. Geophys. Res., 95, 16343–16367, 1990.

798 Stockwell, W. R., Kirchner F., Kuhn M.: A new mechanism for regional atmospheric

799   chemistry modeling, J. Geophys. Res., 102, 25847–25879, 1997.

800 Talbot, R., Dibb, J., Scheuer E., Seid G., Russo R., Sandholm S., Tan D., Singh H.,

801   Blake D., Blake N., Atlas E., Sachse G., Jordan C., Avery M., 2003: Reactive

802   nitrogen in Asian continental outflow over the western Pacific: Results from the

803   NASA Transport and Chemical Evolution over the Pacific (TRACE-P) airborne

804   mission. J. Geophys. Res., 108 (D20), doi:10.1029/2002JD003110, 2003.

805 Tang, Y., Carmichael, G. R., Woo, Jung-Hun, Thongboonchoo N., Kurata, G., Uno,I.,

806   Streets D. G., et al.: Influences of biomass burning during the Transport and

807   Chemical Evolution Over the Pacific (TRACE-P) experiment identified by the

808   regional chemical transport model, J. Geophys. Res., 108(D21), 8824, 2003.

809 Wiedinmyer, C., Akagi, S. K., Yokelson, R. J., Emmons, L. K., Al-Saadi, J.A., Orlando,

810   J. J., and Soja, A. J.: The Fire INventory from NCAR (FINN): a high resolution

811   global model to estimate the emissions from open burning, *Geosci. Model Dev*., **4**,

625-641, doi:10.5194/gmd-4-625-2011, 2011.

Xu, R., Tie, X., Li, G., Zhao, S., Cao, J., Feng T., Long X., Effect of biomass burning on black carbon (BC) in South Asia and Tibetan Plateau: The analysis of WRF-Chem modeling. Science of the Total Environment，645,901-912., 2018.

Yadav, I. C., Devi, N. L., Li, J., Syed, J. H., Zhang, G., Watanabe, H.: Biomass burning in Indo-China peninsula and its impacts on regional air quality and global climate change-a review. Environmental Pollution, 227, 414-427, 2017.

Zhao, C., Liu, X., Leung, L. R. and Hagos, S.: Radiative impact of mineral dust on monsoon precipitation variability over West Africa. *Atmos. Chem. Phys.*, **11**, 1879-1893, 2011.

850 Table 1: WRF-Chem model configuration and physics and chemistry options in this
851 study. (RRTMG=Rapid Radiative Transfer Model for General Circulation Models;
852 FINN=Fire Inventory from National Center for Atmospheric Research)
853

Resolution	10km
Microphysics	Lin
Cumulus parameterization	Grell 3D ensemble scheme
Planetary Boundary Layer	Mellor-Yamada-Janjic TKE scheme
Longwave radiation	RRTMG
Shortwave radiation	RRTMG
Fire emissions	FINN V1.5
Anthropogenic emissions	MICS-Asia III(2010) + Taiwan Emission Data System ver 9.0 (2013)
Biogenic emissions	MEGAN V2.04
Chemistry option	RACM Chemistry with MADE/VBS aerosols using KPP library along with the volatility basis set (VBS) used for Secondary Organic Aerosols
Photolysis option	Madronich
wet scavenging	On , (Neu and Prather, 2012)
Cloud chemistry	On,
feedback from the aerosols to the radiation schemes	On
the time interval for calling the biomass-burning plume rise subroutine	180 min
feedback from the parameterized convection to the atmospheric radiation and the photolysis schemes	On
Subgrid-scale wet scavenging	on
Subgrid aqueous chemistry	on

854
855
856
857
858
859
860
861
862

863 Table 2 Observed and simulated mean values for bias (BIAS), root mean square error
864 (RMSE), and correlation coefficients (R) for EMeRGe HALO flights on 17 and 19
865 March 2018. KET*: the observed Acetone is applied to compare with simulated ketones
866 (KET).

	OBS_ave	SIM_ave	BIAS	RMSE	R
THETA(K)	304.8	304.2	-0.6	1.1	0.99
WS(m/s)	9.1	8.5	-0.6	2.0	0.94
RH(%)	63.6	62.9	-0.6	10.7	0.92
OA(μg/m^3)	1.2	1.4	0.3	1.1	0.61
BC(μg/m^3)	0.4	0.5	0.1	0.4	0.74
SO$_4^{2-}$(μg/m^3)	1.1	2.5	1.4	2.3	0.42
NO$_3^-$(μg/m^3)	0.2	0.6	0.5	2.1	0.31
NH$_4^+$(μg/m^3)	0.4	0.7	0.3	1.2	0.49
CO(ppb)	170.8	191.8	20.9	72.8	0.45
SO$_2$(ppb)	0.2	0.7	0.4	1.2	0.55
O$_3$(ppb)	59.7	63.2	3.5	14.4	0.43
NO$_x$(ppb)	0.2	0.2	0.0	0.2	0.72
NO$_y$(ppb)	1.2	2.6	1.3	2.3	0.03
KET*(ppb)	1.4	1.6	0.1	0.9	0.59
TOL.(ppb)	0.1	0.1	0.0	0.1	0.75
XYL.(ppb)	0.1	0.0	0.0	0.1	0.40
HCHO(ppb)	0.1	0.7	0.5	0.7	0.51
HONO(ppt)	10.5	1.0	-9.4	15.3	0.56

867

868   Table 3 Observed and simulated mean values at an elevation between 2 km and 4 km

869   for bias (BIAS), root mean square error (RMSE), and correlation coefficients (R) during

870   EMeRGe HALO flights on 17 and 19 March 2018. KET*: the observed Acetone is

871   applied to compare with simulated ketones (KET).

	OBS_ave	SIM_ave	BIAS	RMSE	R
THETA(K)	307.5	306.7	-0.7	0.9	0.98
WS(m/s)	8.2	7.9	-0.3	1.7	0.93
RH(%)	55.8	56.0	0.2	7.6	0.96
OA($\mu g/m^3$)	1.3	1.6	0.3	0.7	0.85
BC($\mu g/m^3$)	0.4	0.7	0.2	0.5	0.79
SO_4^{2-}($\mu g/m^3$)	0.8	2.5	1.7	2.1	0.20
NO_3^-($\mu g/m^3$)	0.1	0.0	-0.1	0.3	0.13
NH_4^+($\mu g/m^3$)	0.4	0.4	0.0	0.2	0.52
CO(ppb)	164.4	228.7	64.2	85.4	0.58
SO_2(ppb)	0.0	0.7	0.6	0.9	0.07
O_3(ppb)	60.1	72.6	12.5	15.0	0.55
NO_x(ppb)	0.1	0.2	0.0	0.1	0.53
NO_y(ppb)	1.0	3.6	2.6	3.0	0.51
KET*(ppb)	1.5	2.0	0.5	1.0	0.70
TOL(ppb)	0.1	0.0	0.0	0.1	0.16
XYL(ppb)	0.0	0.0	0.0	0.0	-0.17
HCHO(ppb)	0.1	0.7	0.6	0.7	0.25
HONO(ppt)	6.0	0.6	-5.4	7.2	0.23

872

873

874

875

876

877

878

879

880

881

882

883

884

885

886

887

888

889

890

891

Table 4: Simulated biomass burning contribution (with and without BB emission in Indochina) in percentage (%) on 17 and 19 March, 2018 for different regions: SCA, TWA, ECSA as shown in Figure 1a

895

Average	SCA		TWA		ECSA	
	< 1KM	2-4KM	< 1KM	2-4KM	< 1KM	2-4KM
NO_y	13.6	72.2	39.7	83.3	14.8	69.9
NO_x	-1.3	58.1	2.9	71.1	1.4	51.0
$PM_{2.5}$	7.5	46.0	15.1	55.6	7.6	34.4
OA	5.3	41.4	7.5	48.1	4.4	28.5
BC	8.0	79.5	16.4	81.4	6.8	47.9
OH	14.7	43.8	24.1	67.4	9.2	48.3
O3	18.8	34.2	23.2	39.2	9.2	31.3
CO	9.8	31.7	21.9	38.4	11.1	32.2
KET	6.2	17.8	9.5	27.5	7.2	24.7
HCHO	-4.2	9.8	-4.8	20.6	-4.7	10.4
HO_2	8.8	2.6	15.2	35.8	6.3	23.2
$J(O^1D)$	-1.5	-0.8	-1.1	0.5	-1.5	-1.0

896
897
898
899
900
901
902
903

(a)

905
906
907
908
909
910
911
912
913
914
915
916
917
918
919
920
921

(b)
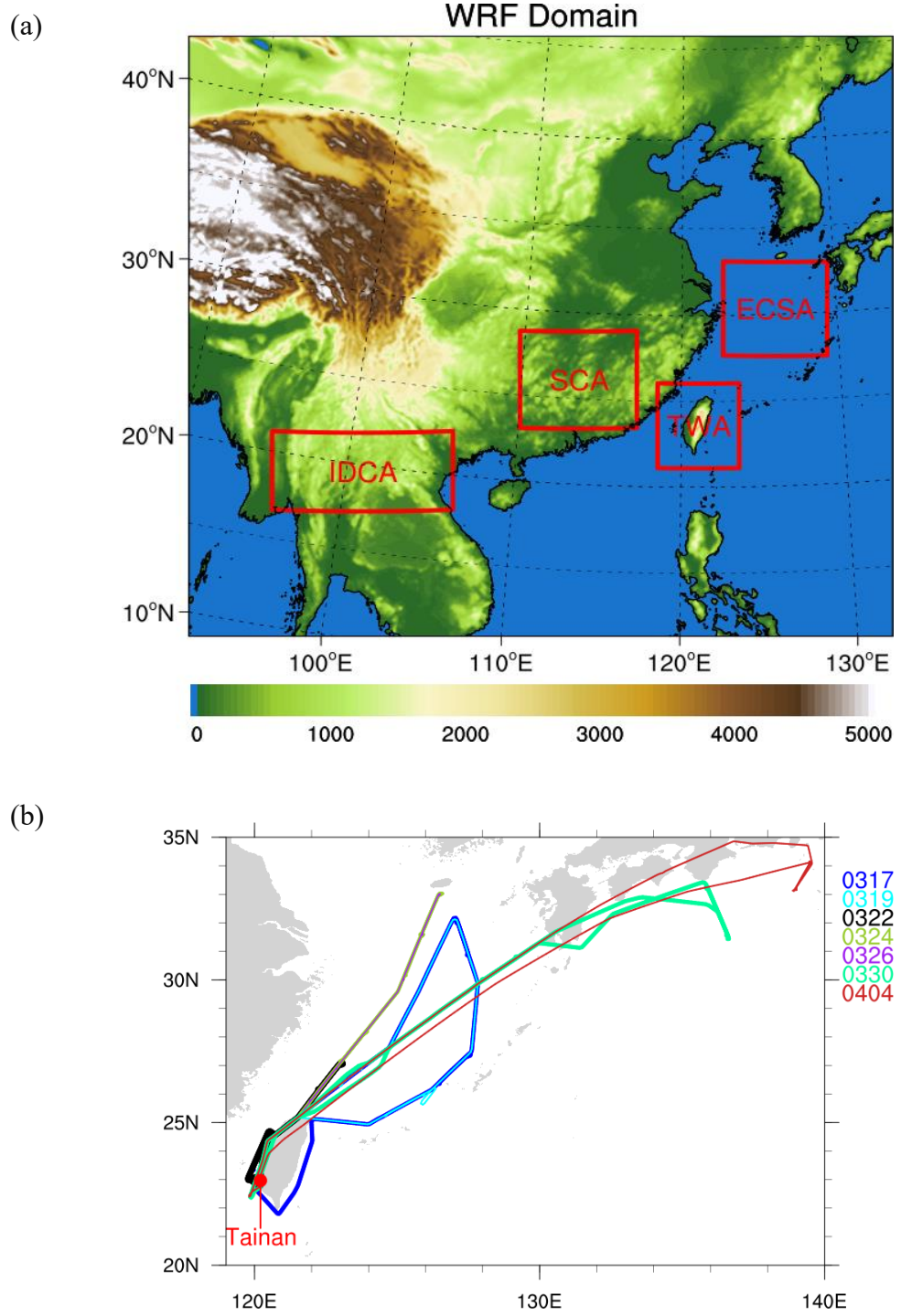
Figure 1 (a) Configuration of Weather Research and Forecasting model domain, topography, and location of proposed study areas in East Asia, namely IDCA (Indochina area), SCA (southern China area), TWA (Taiwan area) and ECSA (East China Sea area, respectively. (b) The HALO flights on 17, 19, 22, 24, 26, 30 March, and 04 April during EMeRGe Asia campaign. Different colors indicated different flights over East Asia. Maps and plots were produced using NCAR Command Language (NCL) version 6.6.2.

942　(a)　　　　　　　　　　　　　　　　　　(b)

943

944　(c)　　　　　　　　　　　　　　　　　　(d)

945
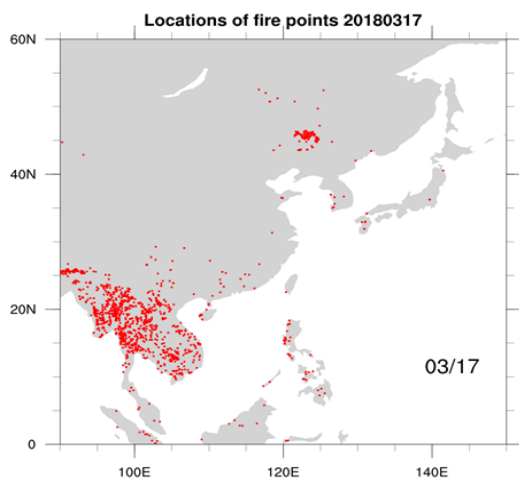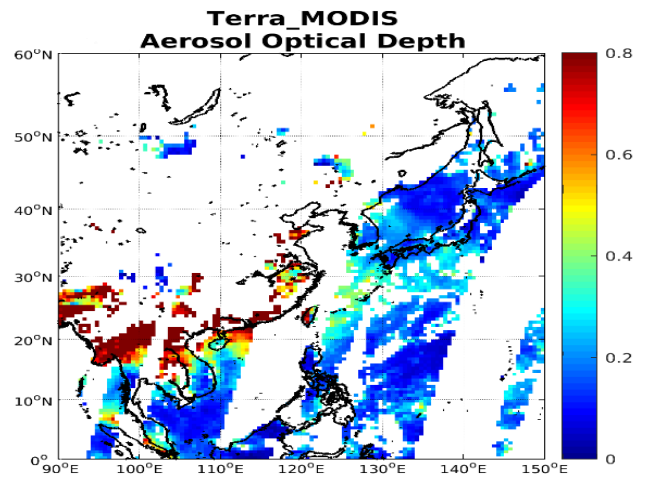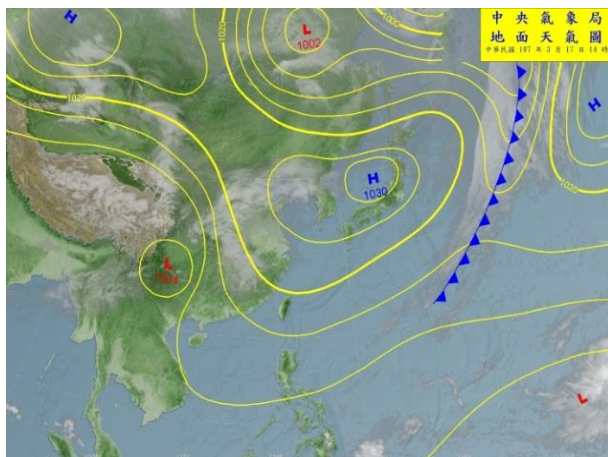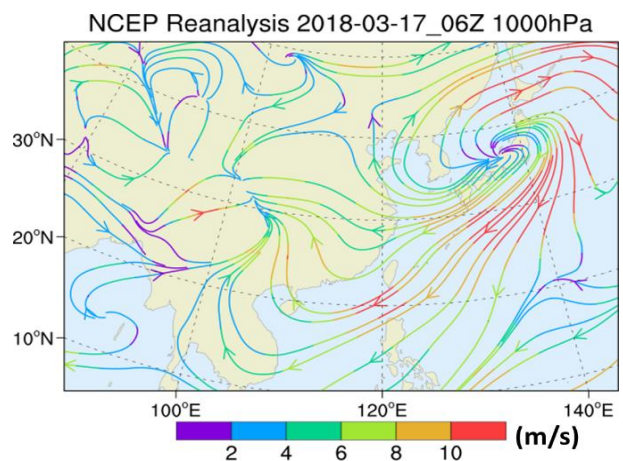
Fig.2　(a) MODIS fire hot spots on 17 March 2018 (source: https://modis-fire.umd.edu/guides.html) and (b) Composited Aerosol Optical Depth (AOD) from MODIS onboard NASA Terra satellite. The Collection 6.1 AOD is downloaded from NASA Earth Data website (https://www.earthdata.nasa.gov/learn/find-data), and composted for 0110, 0115, 0120, 0125, 0130, 0250, 0255, 0300, 0305, 0310, 0430, 0435, 0440, 0445, 0610, 0615, 0620, 0745 and 0750UTC data granules on 17 March 2018. (c) weather Chart at 06:00 UTC on 17 March 2018 (d) 1000 hPa streamlines at 06:00 UTC, 17 March 2018 (e) and (f) same as (c) and (d) but on 19 March 2018 ;(g) 700 hPa streamlines at 06:00 UTC, on 17 March 2018 (h) 700 hPa geopotential height at 06:00 UTC, on 17 March 2018;　(i) and (j) same as (g) and (h) but on 19 March 2018.

Near-surface weather charts and satellite images were provided by Central Weather Bureau (CWB) Taiwan. The near-surface and 700 hPa streamlines and geopotential height were deduced from NCEP Reanalysis data. Maps and plots were produced using NCAR Command Language (NCL) version 6.6.2.

961   (e)   (f)

962

963

964   (g)   (h)
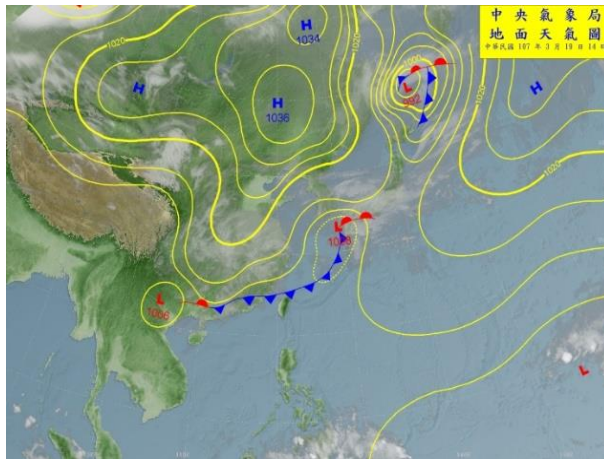
965
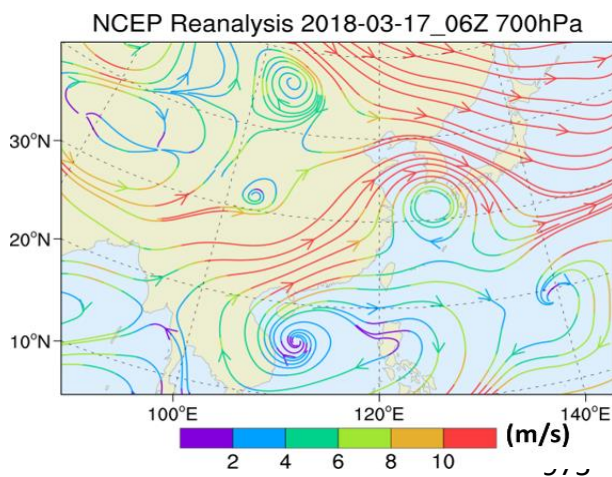
976

977

978

979   Figure 2 e-h continued

980

981

982

983

984

985

986

987

988

989   (i)   (j)

990

991

NCEP Reanalysis 2018-03-19_06Z 700hPa   NCEP Reanalysis 2018-03-19_06Z 700hPa

992
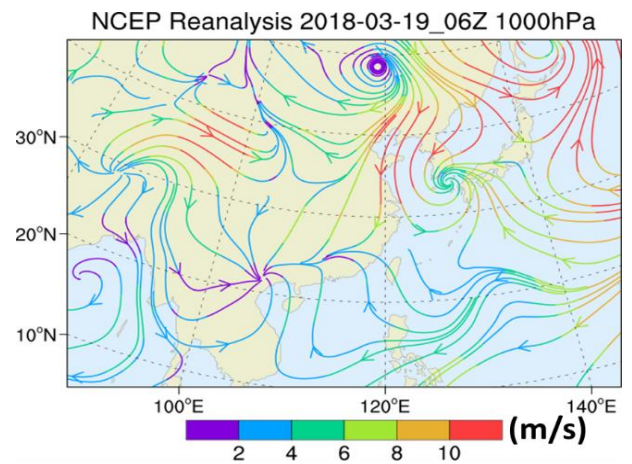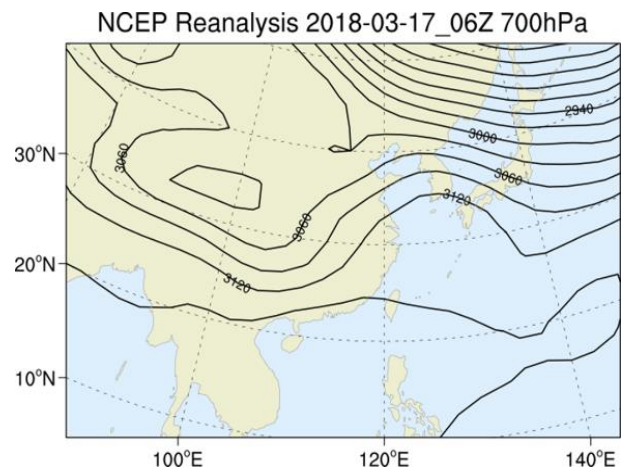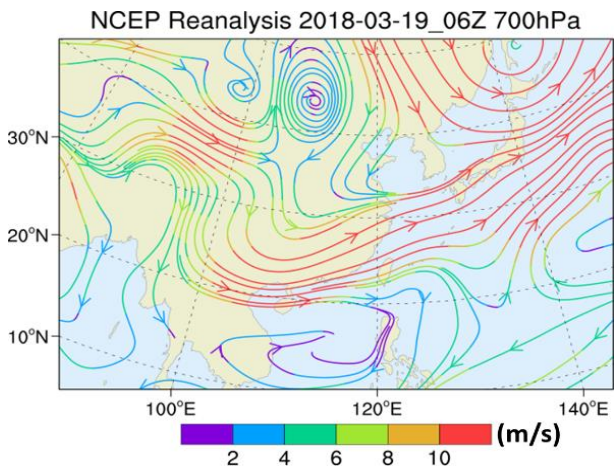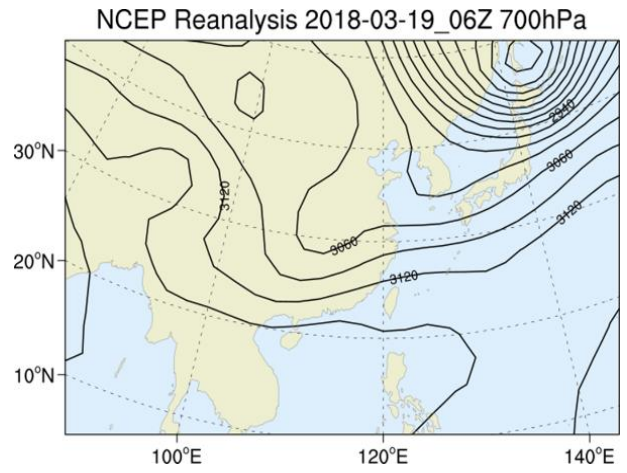
993

994

995

996

997

998

999

1000

1001

1002

1003

1004

1005

1006   Fig. 2 i-j continued

1007

1008

1009

1010

1011

1012

1013

1014

1015

1016

1017

1018   (a)   (b)

CO diff@20180317_00Z UTC   CO diff@20180317_12Z UTC

1019

1020   (c)   (d)

CO diff@20180317_00Z UTC   CO diff@20180317_12Z UTC

1021

1022   (e)

Backward traj. Starting at 00 UTC 17 Mar. 2018
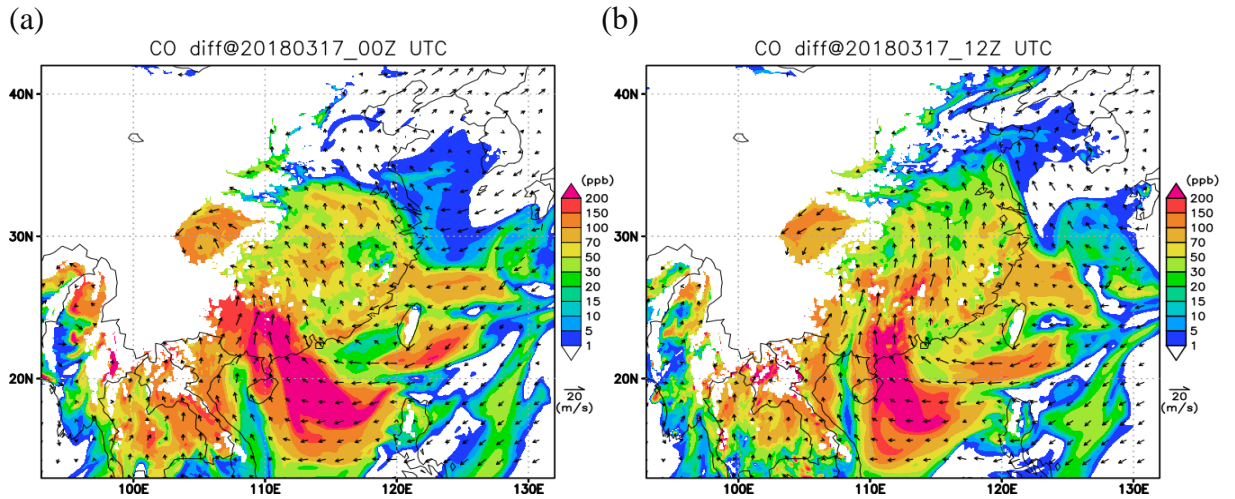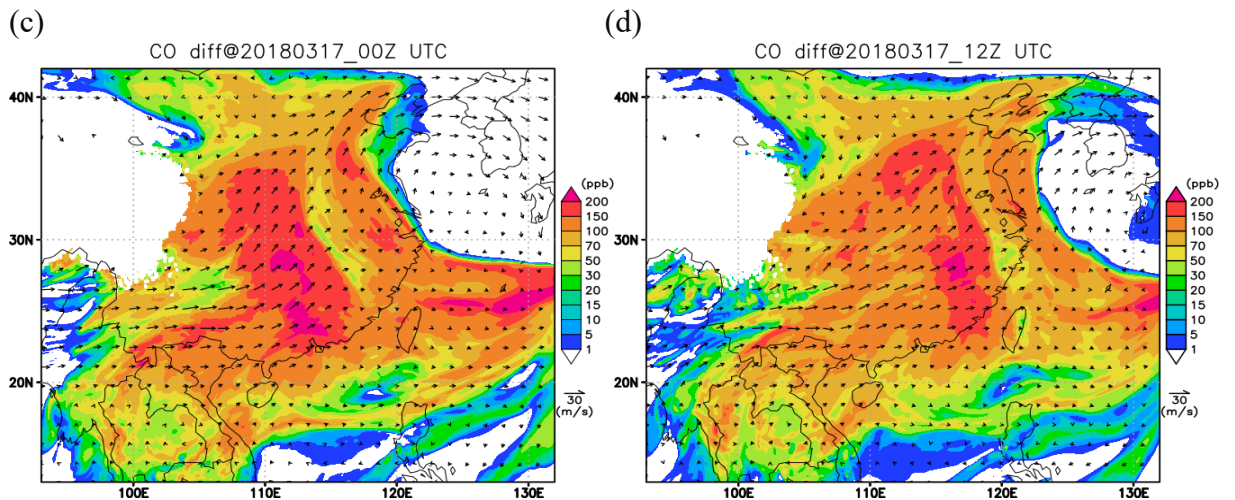
1023
1024
1025
1026
1027
1028
1029
1030
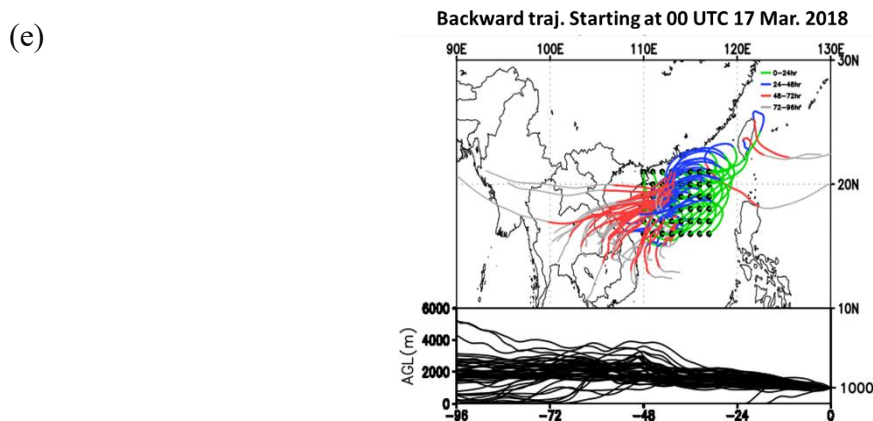
1031   Fig 3. Simulated wind field (m s^{-1}) distribution and concentration (unit: ppb) difference

1032   with and without BB emission for CO on 17 March, 2018 at 00:00 UTC (a, c) and 12:00

1033   UTC (b, d) for 1km altitude (a, b) and 3km altitude (c, d). (unit: ppb). (e) The results of

1034   the HYSPLIT model backward trajectory analysis at 1000 meters with multiple points

1035   by 1˚X1˚ in the area (110-115˚E, 17.5-22.5 ˚N) of East China Sea started at 00:00 UTC

1036   17 March 2018.

39

1037 (e)

CO diff@20180319_00Z UTC

(f)

CO diff@20180319_12Z UTC

1038

1039 (g)

CO diff@20180319_00Z UTC

(h)

CO diff@20180319_12Z UTC

1040

1041 (e)

Backward traj. Starting at 04 UTC 19 Mar. 2018
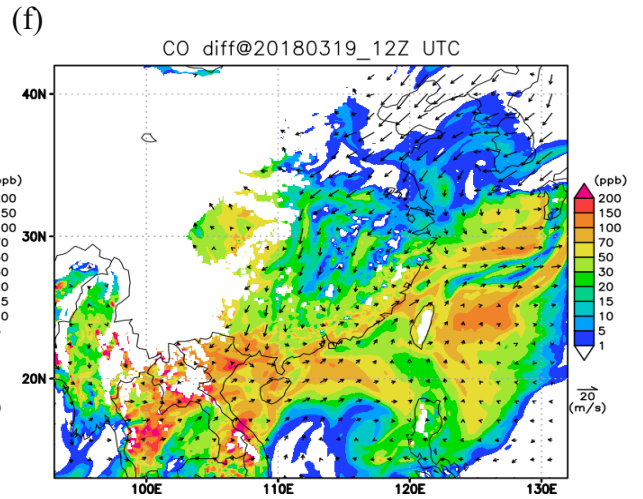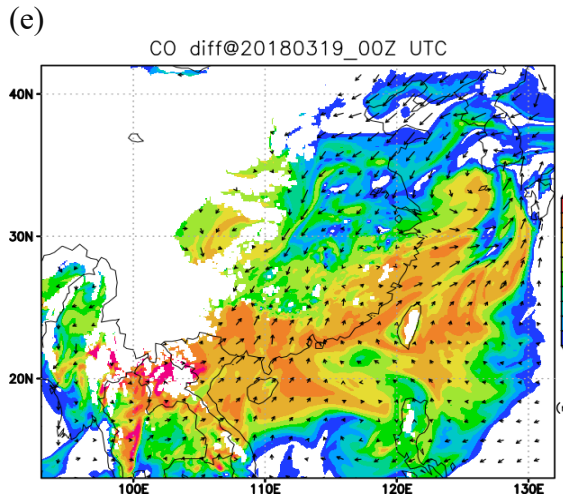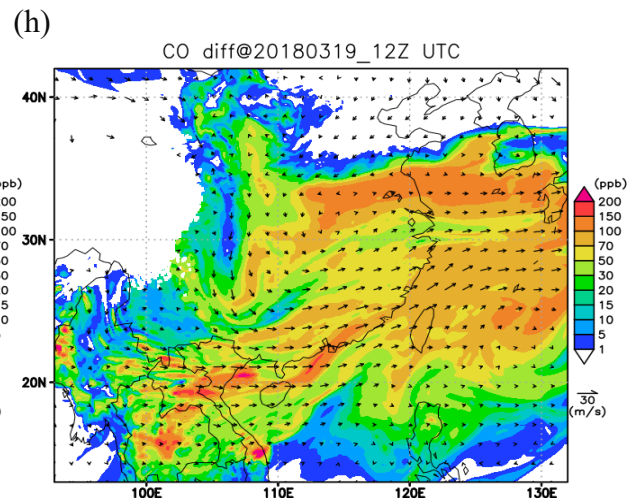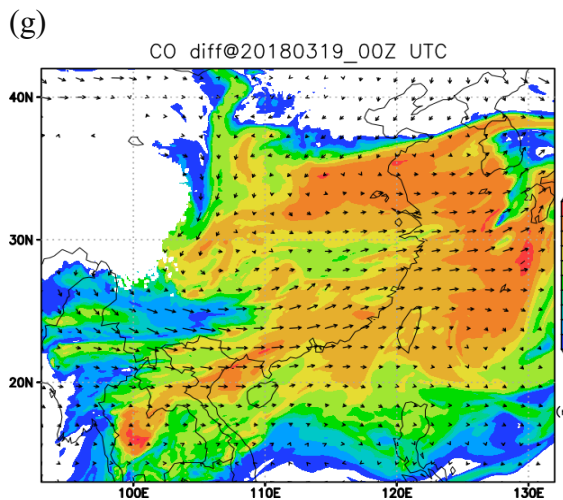
1042

1043

1044

1045

1046

1047

1048

1049

1050
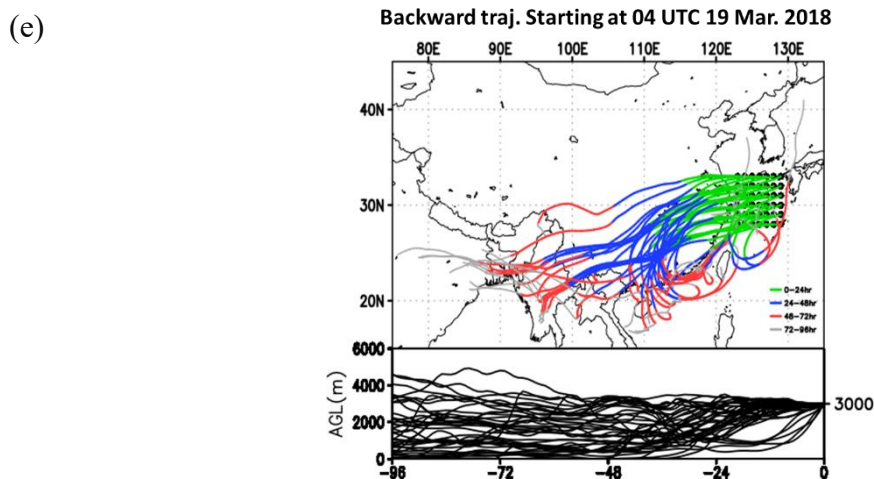
1051 Fig 4 Simulated wind field (m s^{-1}) and concentration (unit: ppb) difference with and

1052 without BB emission for CO on 19 March, 2018 at 00:00 UTC (e, g) and 12:00 UTC

1053 (f, h) for 1km altitude (e, f) and 3km altitude (g, h).   (e) The results of the HYSPLIT

1054 model backward trajectory analysis at 3000 meters with multiple points by 1˚X1˚ in the

1055 area (122-130˚E, 28-33 ˚N) of East China Sea started at 04:00 UTC 19 March 2018.

1056

1057

1058

1059 (a)

CO diff@20180318_16Z UTC

1060

1061

1062

1063

1064

1065

1066

1067 (b)

CO diff@20180319_06Z UTC
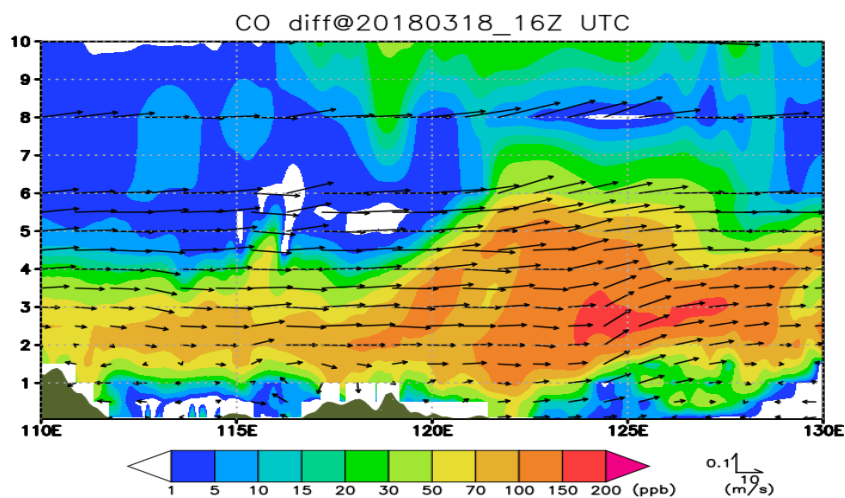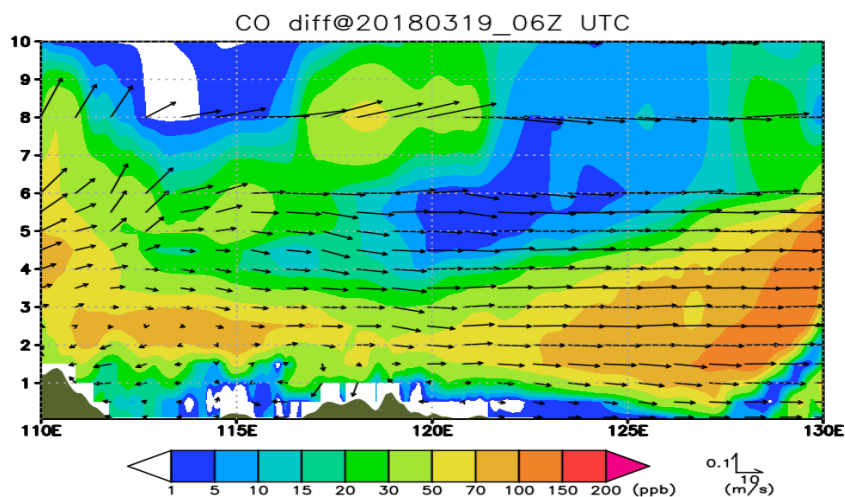
1068

1069

1070

1071

1072 Fig. 5 Simulated wind field (m s^{-1}) distribution and the concentration (ppb) difference

1073 between with and without BB emission for CO at cross-section 30 °N (a) 16:00 UTC

1074 18 March 2018 (b) 06:00 UTC, 19 March 2018. Wind vectors represent along section

1075 winds, with scales shown at the down-right corner of plot (unit: m s^{-1})

1076

1077

1078

1079

(a)

(b)
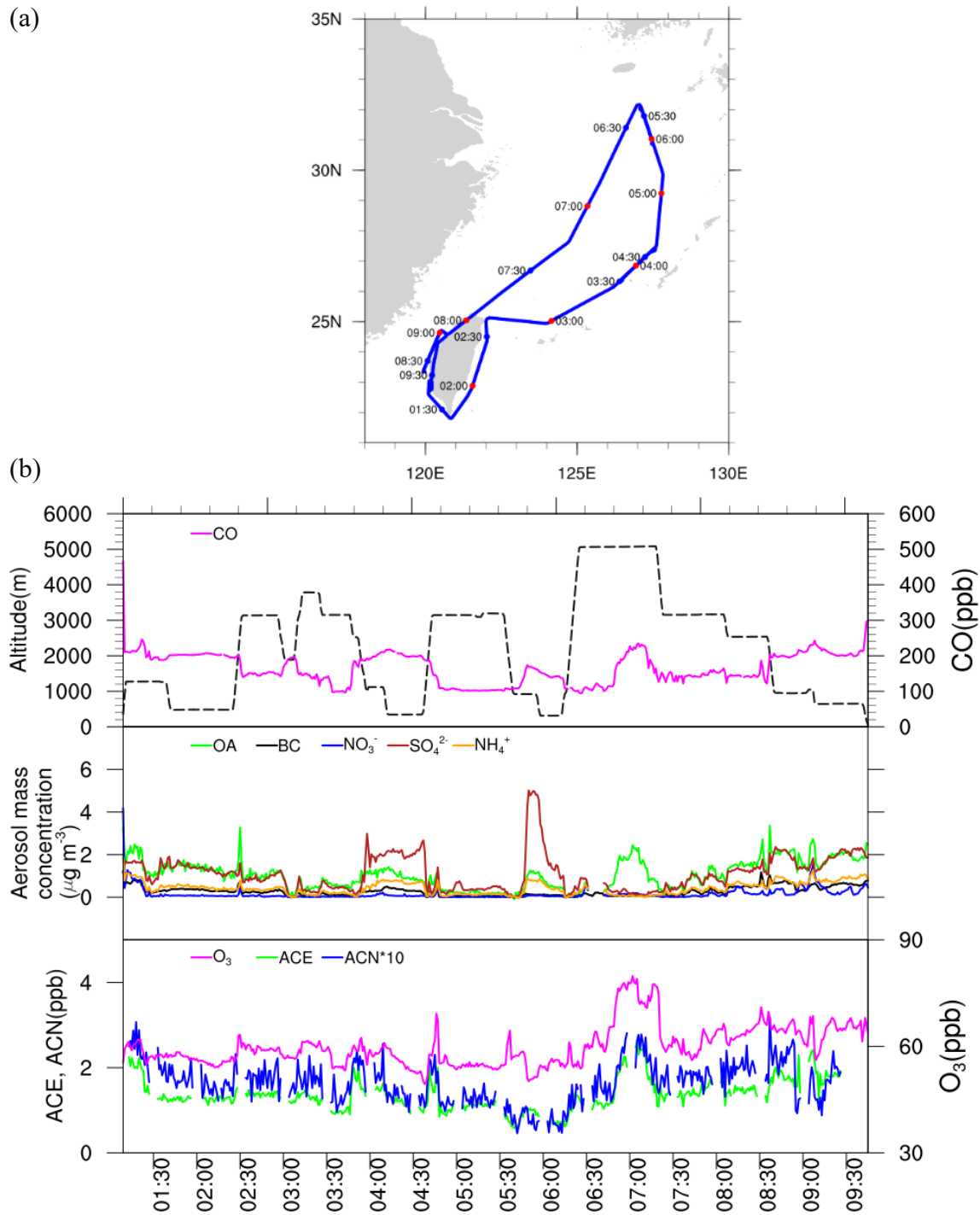
Fig. 6 (a) The HALO flight and detailed locations on 17 March 2018. (b) Flight altitude and 1-min mean of observed concentrations for CO (upper), Organic aerosol (OA), BC aerosol (BC), SO_4^{2-}, NO_3^-, NH_4^+ (middle), O_3, acetone (ACE) and acetonitrile (ACN) (bottom) on 17 March.   (c) The observed SO_4^{2-} mass concentration by HALO along with height-latitude variations on 17 March 2018 (d) The observed OA mass concentration by HALO along with height-latitude variations on 17 March 2018 (e) Result of the HYSPLIT model backward trajectory analysis started at the location of the HALO flight path at 02:00, 04:00, 06:00, 09:00 UTC on 17 March 2018.
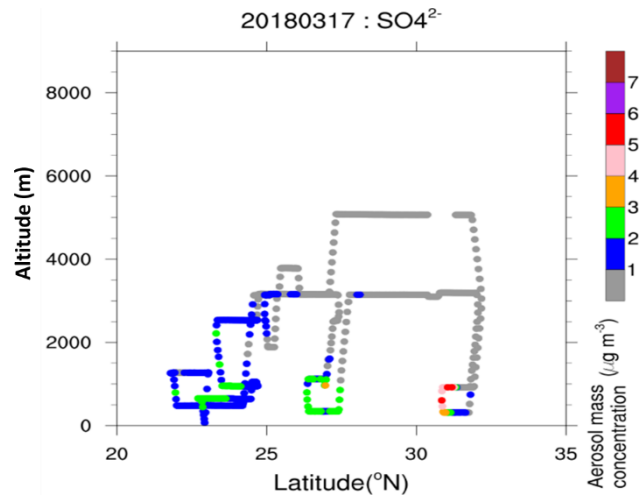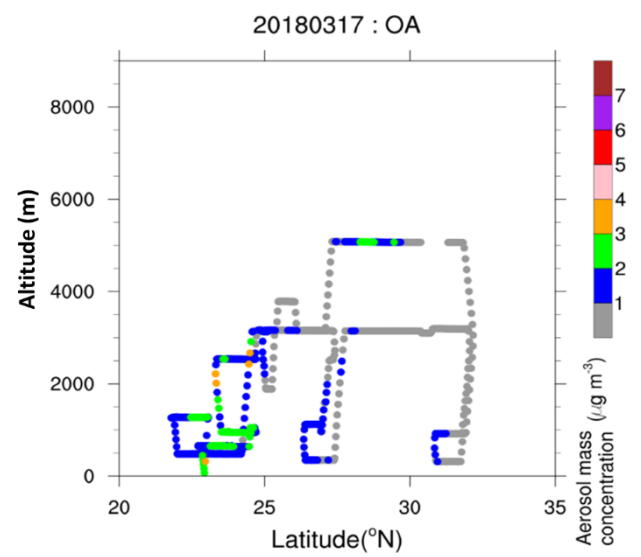
(c)

20180317 : SO4²⁻

(d)

20180317 : OA

(e)

Case 0317_REANALYSIS

Figure 6 c-e

(a)

(b)
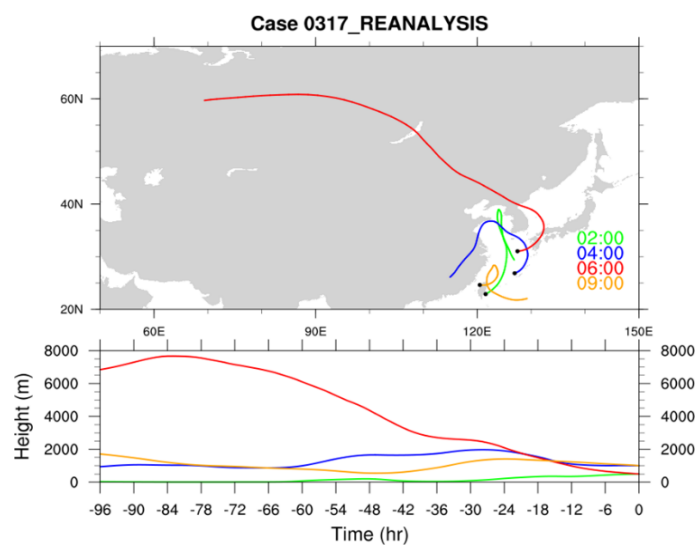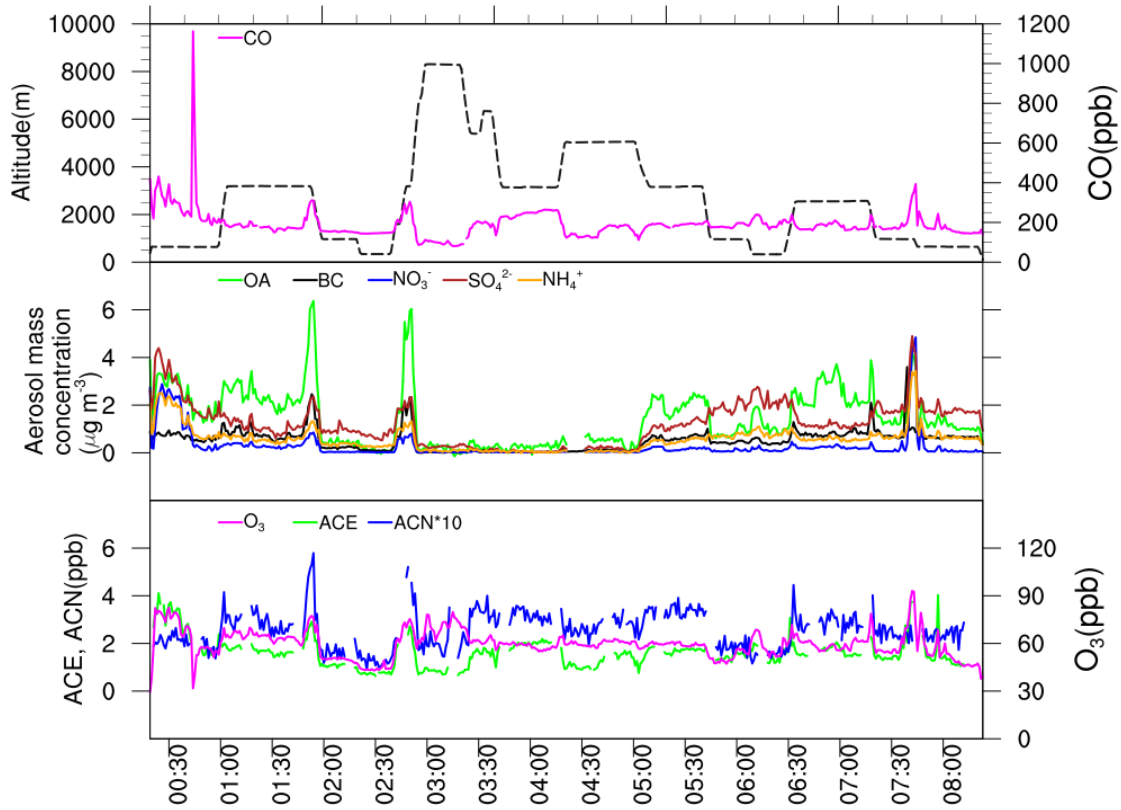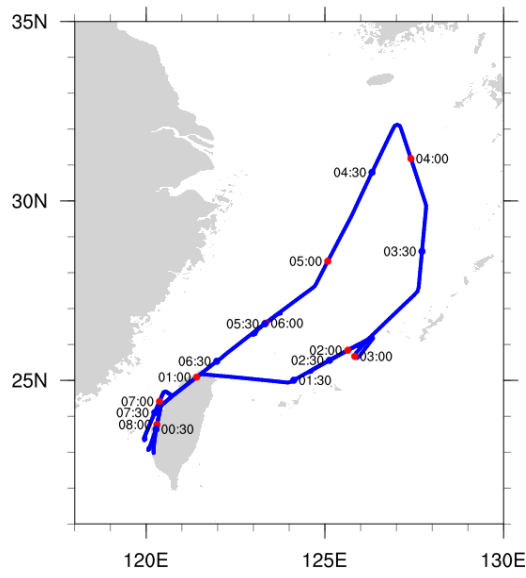
Figure 7 (a) The HALO flight and detailed locations on 19 March. (b) Flight altitude and 1-min mean of observed concentrations for CO (upper), Organic aerosol (OA), BC aerosol (BC), SO_4^{2-}, NO_3^-, NH_4^+ (middle), O3, acetone (ACE) and Acetonitrile (ACN) (bottom) on 19 March 2018.　(c) The observed SO_4^{2-} mass concentration by HALO along with height-latitude variations on 19 March 2018 (d) The observed OA mass concentration by HALO along with height-latitude variations on 19 March 2018 (e) Result of the HYSPLIT model backward trajectory analysis started at the location of the HALO flight path at 02:00, 04:00, 05:00, 07:00 UTC on 19 March 2018.
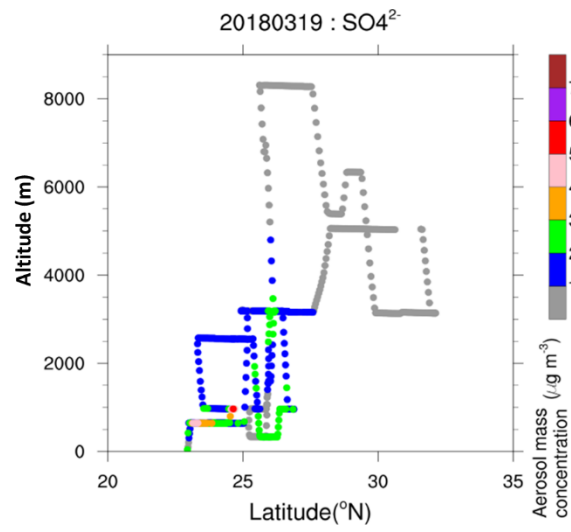
(c)

(d)

(e)
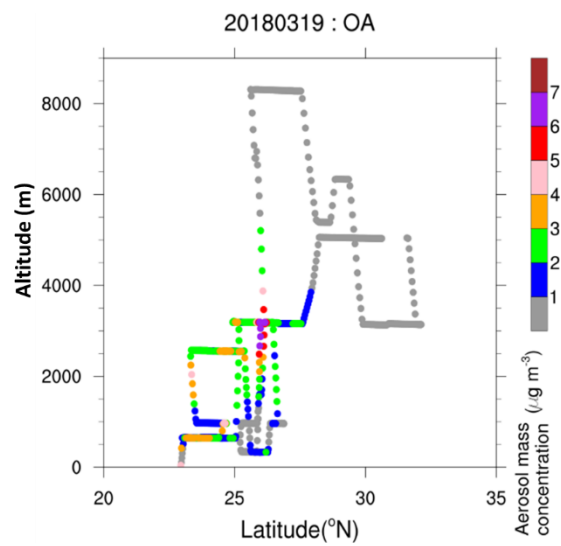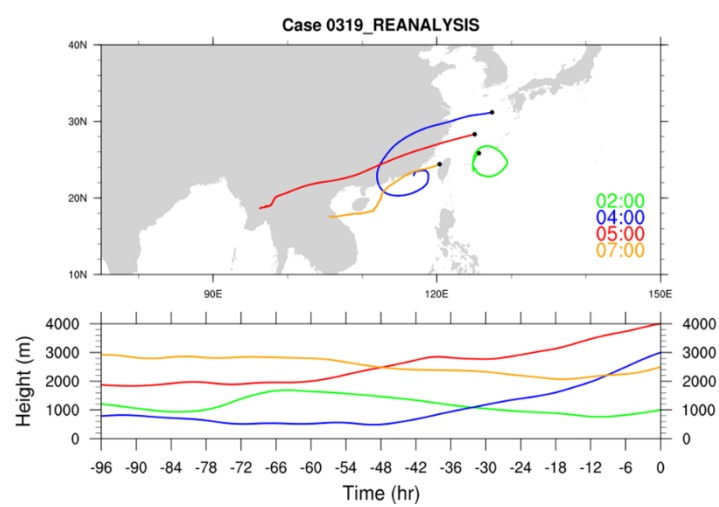
Figure 7 c-e

1199   (a)   (b)

1200
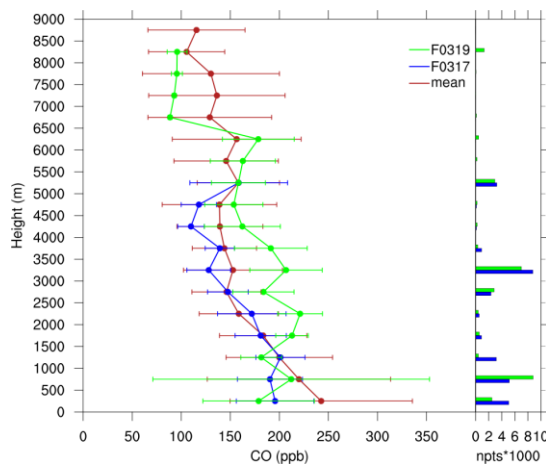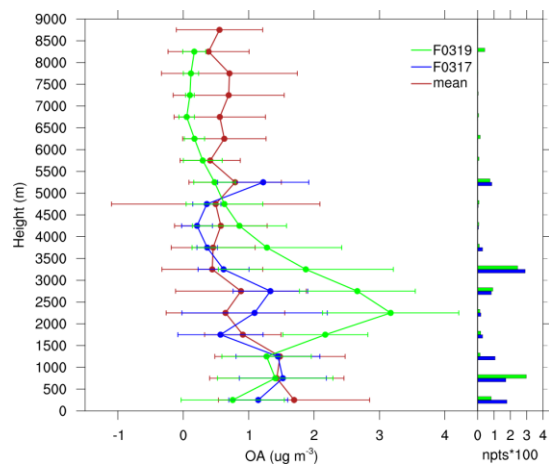
1201
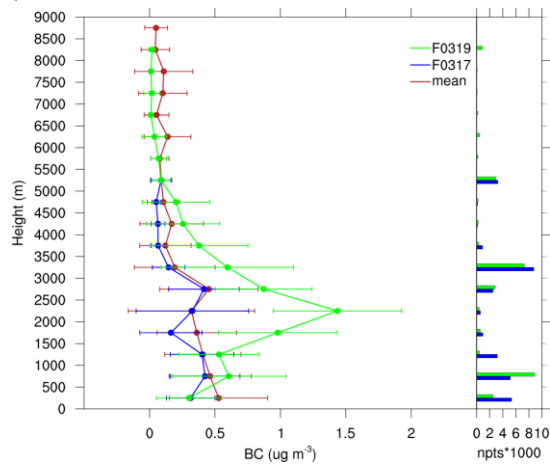
1202   (c)   (d)
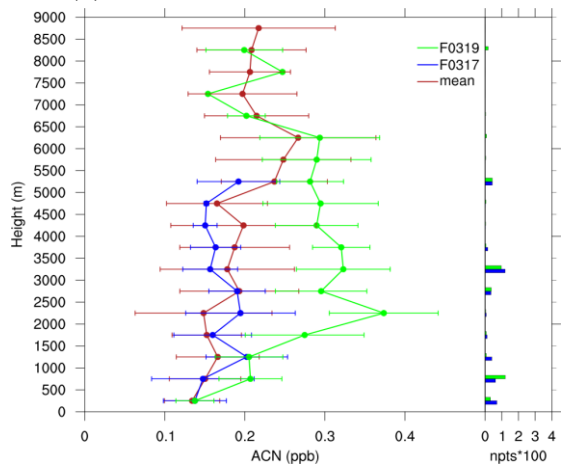
1203

1204

1205

1206

1207   Fig.8 Observed vertical distribution calculated as 1-min mean and 500 m interval with
1208   one standard deviation of the concentrations for the mean profiles (red) (including 17,
1209   19, 22, 24, 26, 30 March, and 04 April 2018) and flights on 17 (blue) and 19 (green)
1210   March 2018. (a) CO (b) OA (c) BC (d) Acetonitrile (ACN) (e) Acetone (ACE) (f) O_3
1211   (g) J (O^1D) (h) NO_y. The number of data points is shown in the right panel.

1212

1213

1214 (e)
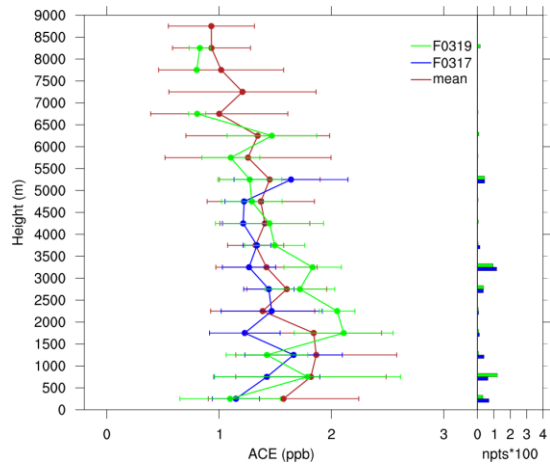
(f)
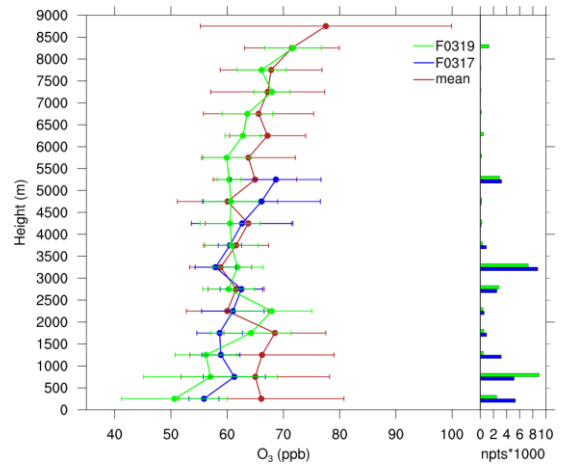
1215

1216 (g)
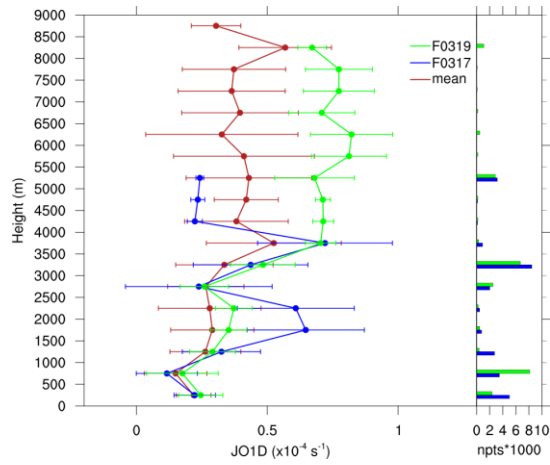
(h)
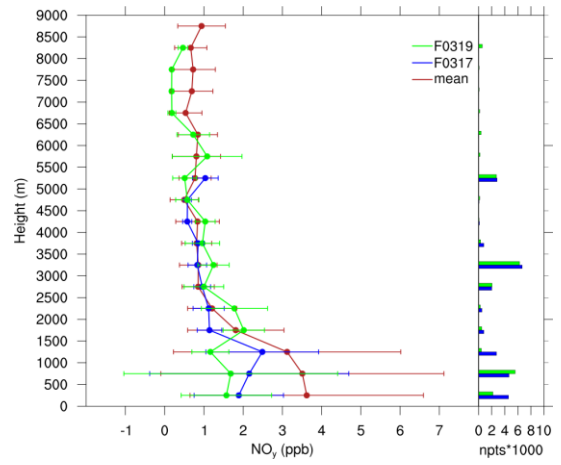
1217

1218

1219

1220

1221

1222

1223 Fig. 8 continued

1224

1225

1226

1227

1228

1229

1230

1231

0317&19
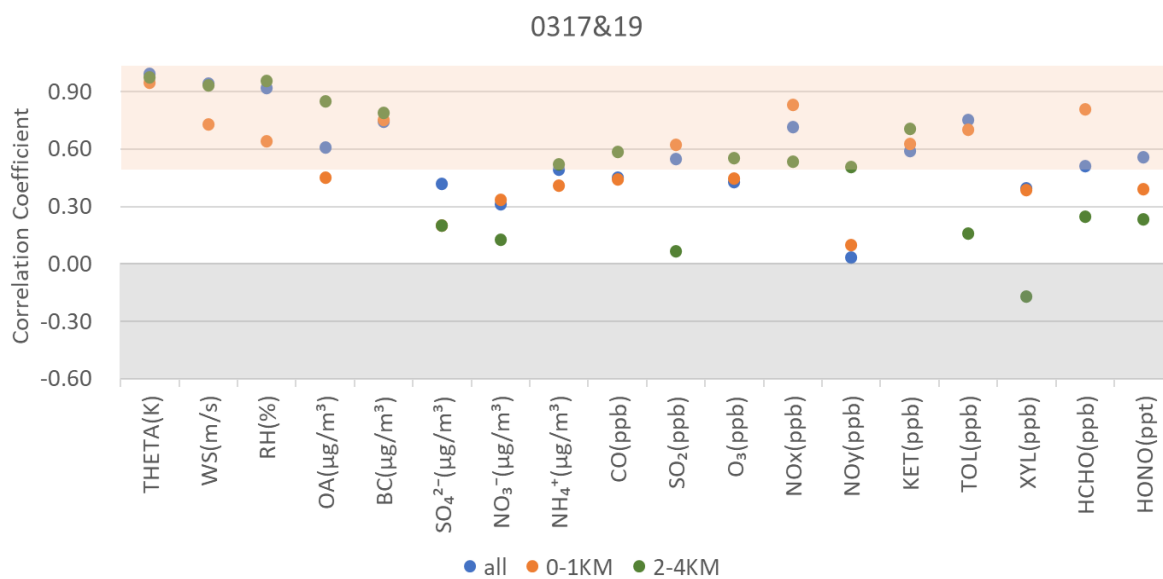
1232

1233

1234

Fig. 9   Correlation Coefficient (R) between observation and simulation along with the
HALO flights at the elevations 0-1 km, 2-4 km, and the whole track (all) on 17 and 19
March 2018.

1238

1239

1240

1241

1242

1243

1244

1245

1246

1247

1248

1249

1250

1251

1252

1253

1254

1255

1256

1257 (a)

1268 (b)
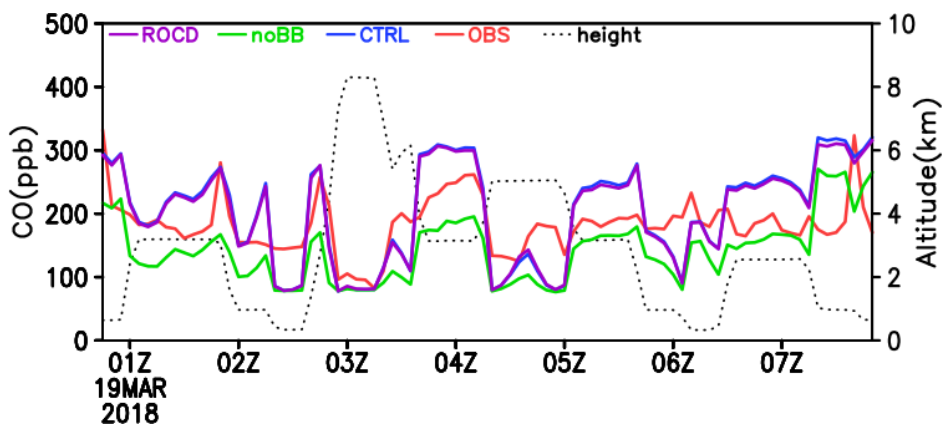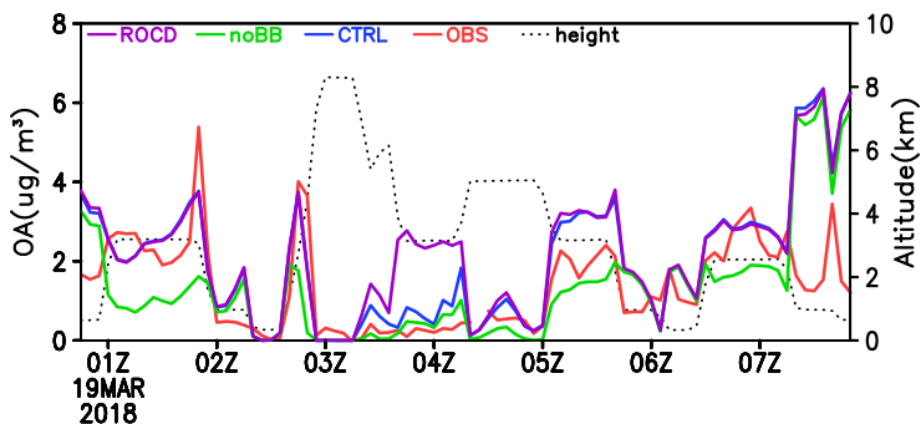
1279 (c)
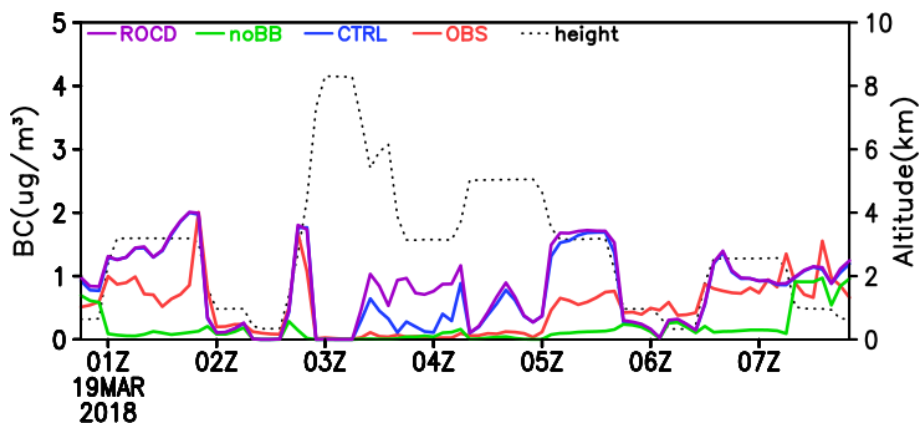
1291 Fig.10   Observed (OBS, red) and simulated concentration (CTRL, blue), and the simulation
1292 without indirect effect (ROCD, purple), without BB emission (noBB, green) along with the
1293 flight altitude for (a) CO (ppb) (b) OA (μg m^{-3}) (c) BC (μg m^{-3}) on 19 March 2018.
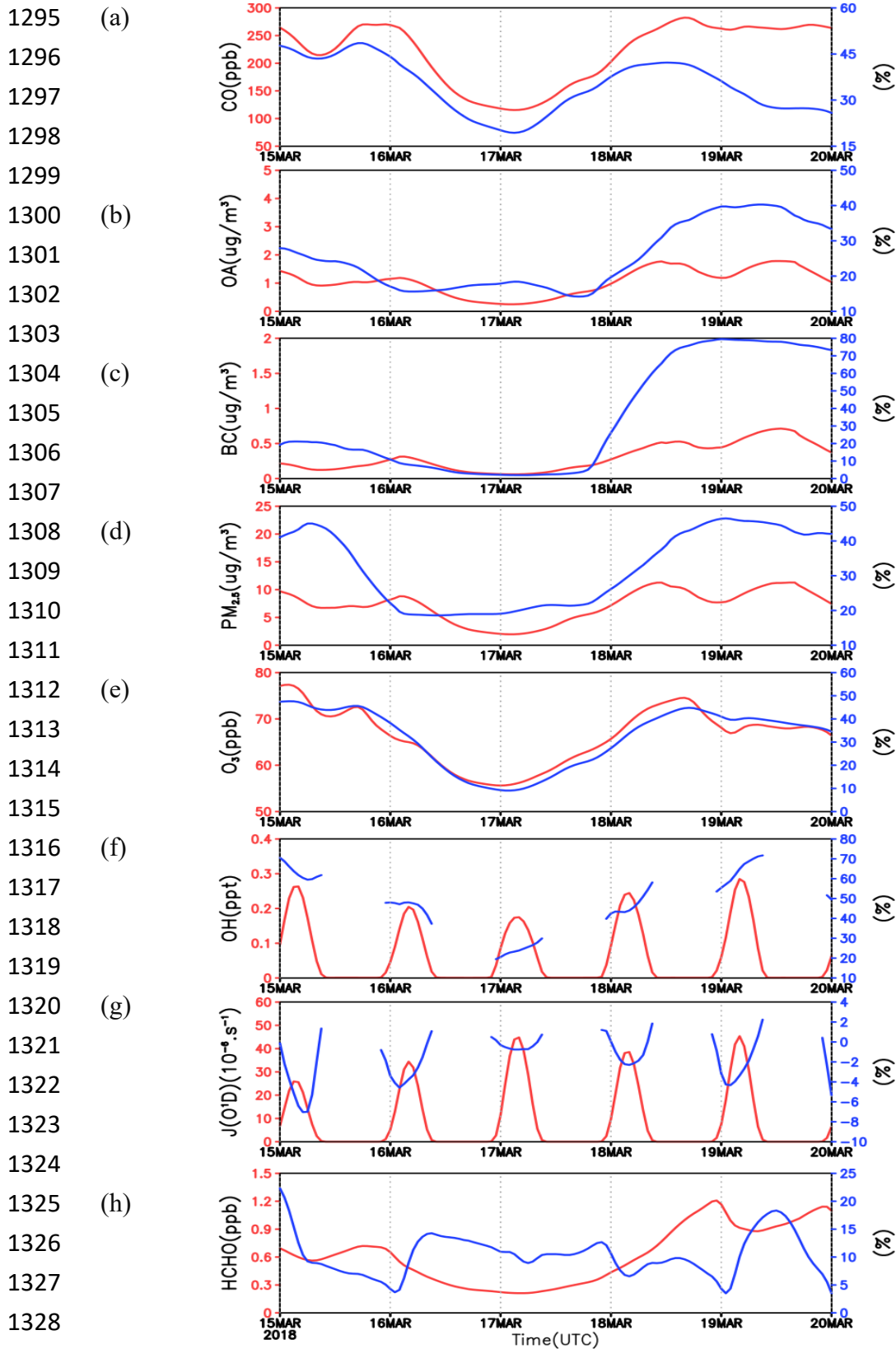
Fig. 11 Hourly variation of simulated mean concentration (red) and contributed by BB (%, blue) between 2 km and 4 km over the region ECSA in Fig.1a during 15-19 March 2018. (a) CO (b) OA (c) BC (d) PM$_{2.5}$ (e)O$_3$ (f) OH (g) J(O^{1}D), and (h) HCHO

(a)

(b)
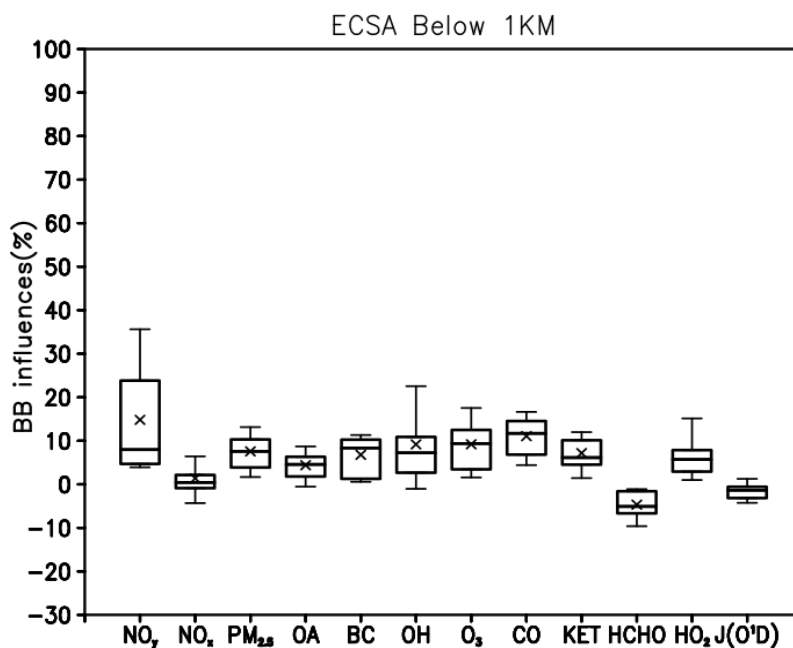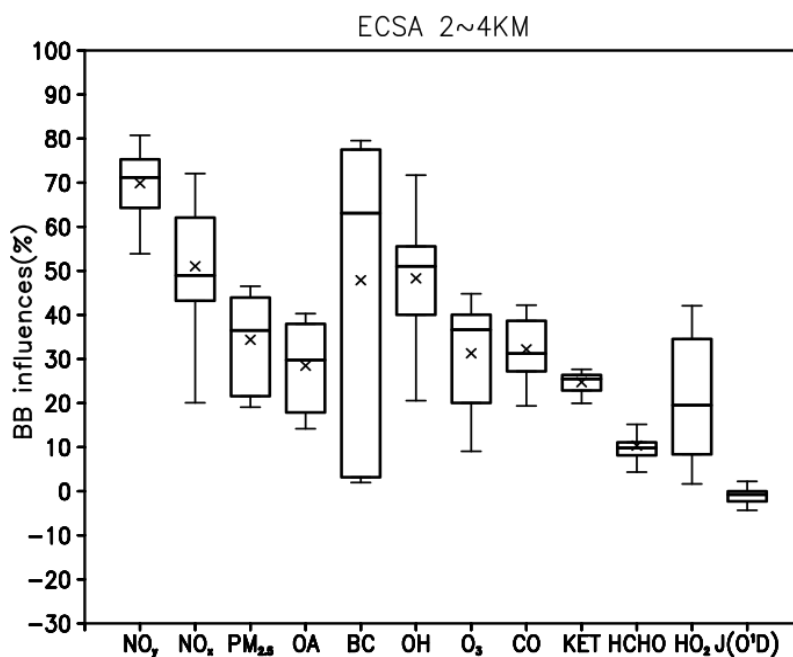
Fig. 12 Box plots of simulated BB influences (%) on NO_y, NO_x, $PM_{2.5}$, OA, BC, OH, O_3, CO, KET, HCHO, HO_2 ,and $J(O^1 D)$ over the region ECSA in Fig. 1a on 17 and 19 March 2018. (a) below 1 km, (b) between 2 km and 4 km

1371 (a)

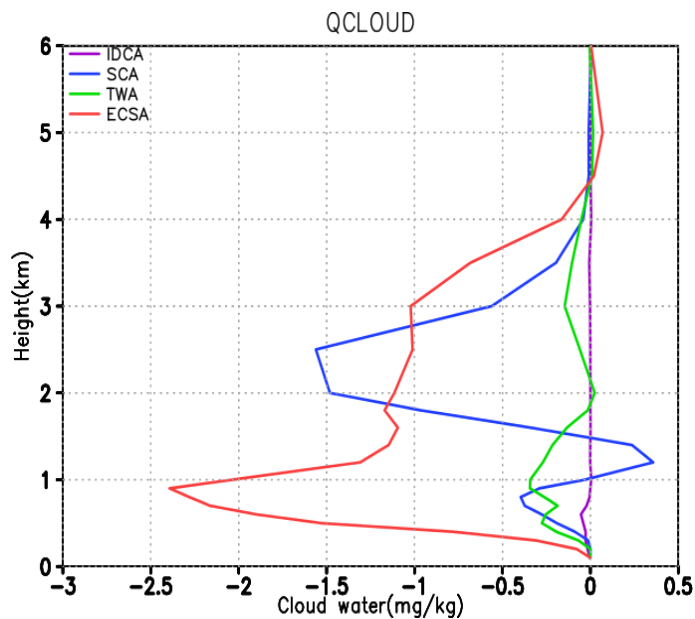

1386 (b)
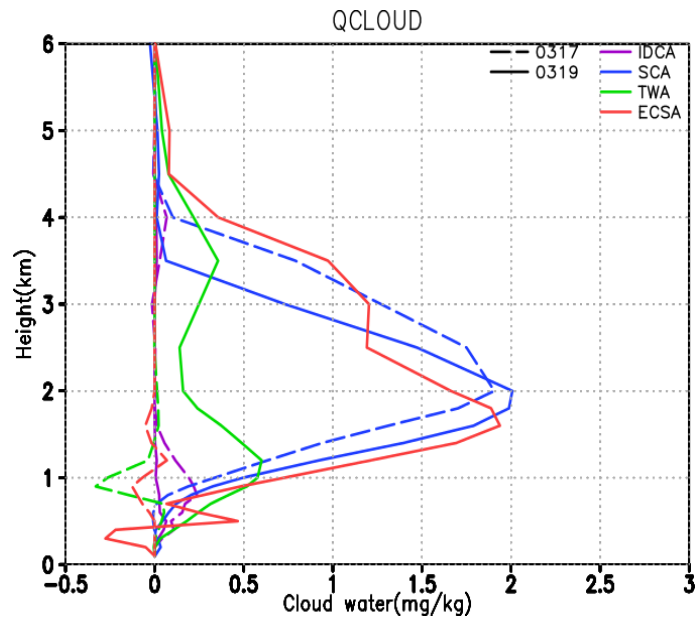
Fig. 13 (a) Simulated vertical distribution of BB influences on cloud water difference between with and without BB emission on 17 (dash) and 19 (solid) March 2018. (b) Simulated vertical distribution of cloud water difference between with and without indirect effect in the model on 19 March 2018.

Regions include IDCA, SCA, TWA, and ECSA as shown in Figure 1a.